"Variational Transition State Theory in the Treatment of Hydrogen Transfer Reactions," D. G. Truhlar and B. C. Garrett, in Hydrogen Transfer Reactions, edited by J. T. Hynes, J. P. Klinman, and H.-H. Limbach, and R. L. Schowen (Wiley-VCH, Weinheim, Germany, 2007), Vol. 2, pp. 833-874.

27
Variational Transition State Theory in the Treatment of Hydrogen Transfer Reactions

Donald G. Truhlar and Bruce C. Garrett

27.1
Introduction

Transition state theory (TST) [1–4] is a widely used method for calculating rate constants for chemical reactions. TST has a long history, which dates back 70 years, including both theoretical development and applications to a variety of reactions in the gas phase, in liquids, at interfaces, and in biological systems. Its popularity and wide use can be attributed to the fact that it provides a theoretical framework for understanding fundamental factors controlling chemical reaction rates and an efficient computational tool for accurate predictions of rate constants.

TST provides an approximation to the rate constant for a system where reactants are at equilibrium constituted by either a canonical ensemble (thermal equilibrium) or a microcanonical ensemble (corresponding to a fixed total energy). Two advances in TST have contributed significantly to its accuracy: (i) the variational form of TST in which the optimum dividing surface is determined to minimize the rate constant and (ii) the development of consistent methods for treating quantum mechanical effects, particularly tunneling. TST in a classical mechanical world can be derived by making one approximation – Wigner's fundamental assumption [3]. With this assumption, the net reactive flux through a dividing surface separating reactants and products is approximated by the equilibrium one-way flux in the product direction. In a classical world this approximation leads to an overestimation of the rate constant, since all reactive trajectories are counted as reactive, but some nonreactive ones also contribute to the one-way flux. In variational TST (VTST), the dividing surface is optimized to give the lowest upper bound to the true rate constant [5–7].

The need to include quantum mechanical effects in reaction rate constants was realized early in the development of rate theories. Wigner [8] considered the lowest order terms in an $\hbar$-expansion of the phase-space probability distribution function around the saddle point, resulting in a separable approximation, in which bound modes are quantized and a correction is included for quantum motion along the reaction coordinate – the so-called Wigner tunneling correction. This separable approximation was adopted in the standard *ad hoc* procedure for quan-

Hydrogen-Transfer Reactions. Edited by J. T. Hynes, J. P. Klinman, H. H. Limbach, and R. L. Schowen

ISBN: 978-3-527-30777-7

tizing TST [1]. In this approach, partition functions for bound modes are treated quantum mechanically, usually within a harmonic approximation, and a correction for tunneling through the potential barrier along the reaction coordinate is included. Even though more accurate treatments of tunneling through parabolic barriers have been presented [9], beyond the expansion through $\hbar^2$ of Wigner, tests of TST using accurate quantum mechanical benchmarks have shown that this nonseparable approximation is inadequate for quantitative predictions of rate constants when quantum mechanical effects are important [10, 11].

Breakthroughs in the development of quantum corrections for VTST, particularly tunneling, came from comparing the adiabatic theory of reactions [12–14] with VTST for a microcanonical ensemble (microcanonical variational theory). Even though the two theories are based upon very different approximations, they predict the same reaction rates when the reaction coordinate is defined in the same way in both theories and motion perpendicular to it is treated classically [7] or by an identical quantum mechanical approximation [15]. Consequently, quantum mechanical treatments of reaction-coordinate motion for the adiabatic theory provide a starting point for developing quantal corrections for VTST that include the nonseparable, multidimensional nature of tunneling [16–24]. In these approaches, the multidimensional character of the tunneling is included by specifying an optimal tunneling path through the multidimensional space. This approach was pioneered by Marcus and Coltrin [25], who developed the first successful nonseparable tunneling correction for the collinear H + H_2 reaction, for which only one mode is coupled to the reaction coordinate.

H-transfer reactions are of great interest because they play important roles in a variety of systems, from gas-phase combustion and atmospheric reactions of small molecules to complex catalytic and biomolecular processes. Many enzyme reactions involve proton or hydride transfer in the chemical step [26], and we know from experience with simpler reactions that multidimensional treatments of the tunneling process are essential for quantitative accuracy and sometimes even for qualitative understanding.

From a theoretical point of view H transfer reactions are of great interest because they provide opportunities to study the importance of quantum mechanical effects in chemical reactions and are a good testing ground to evaluate approximate theories, such as TST approaches. There is a long history of applications of TST to H-transfer reactions starting with the H + H_2 reaction and its isotopic variants. A comprehensive review of the early literature for the H + H_2 reaction appeared over 30 years ago [27]. In the 1960s it was being debated whether quantum mechanical tunneling was important in the H + H_2 reaction (see Ref. [28], pp. 204–206]). Since then studies on gas-phase H-atom transfer reactions, particularly using TST methods, have shown definitively that treatment of quantum mechanical effects on both bound modes and reaction coordinate motion is important in the treatment of light-atom transfer reactions, such as hydrogen atom, proton, and hydride transfers. This point is strongly supported by two comprehensive reviews of TST and applications of TST approaches to chemical reactions, including H transfer, that have been published over the past 20 years [4].

Kinetic isotope effects (KIEs) have played an important role in using experiments to unravel mechanisms of chemical reactions from experimental data [29]. The primary theoretical tool for interpreting KIEs is TST [29, 30]. The largest KIEs occur for hydrogen isotopes, for which it is critical to consider quantum mechanical effects. It has also been shown that effects of variationally optimizing the dividing surface can have significant effects on primary hydrogen KIEs [31]. VTST with multidimensional tunneling (MT) provides a more complete theory of kinetic isotope effects, which has recently been demonstrated by its ability to predict kinetic isotope effects in complex systems, such as hydride transfer in an enzymatic reaction [32].

Calculations of reaction rates with variationally determined dynamical bottlenecks and realistic treatments of tunneling require knowledge of an appreciable, but still manageably localized, region of the potential energy surface [33]. In this chapter we assume that such potentials are available or can be modeled or calculated by direct dynamics, and we focus attention on the dynamical methods.

In this chapter we provide a review of variational transition state theory with a focus on how quantum mechanical effects are incorporated. We use illustrative examples of H-transfer reactions to assist in the presentation of the concepts and to highlight special considerations or procedures required in different cases. The examples span the range from simple gas-phase hydrogen atom transfer reactions (triatomic to polyatomic systems), to solid-state and liquid-phase reactions, including complex reactions in biomolecular enzyme systems.

27.2 Incorporation of Quantum Mechanical Effects in VTST

An important consideration in developing variational transition state theory is the definition of the dividing surface separating reactants from products. A convenient choice is to consider a one-parameter sequence of dividing surfaces that are defined to be orthogonal to a reaction path [7, 34], rather than to allow more arbitrary definitions. This procedure has a few advantages. First, the variational optimization is performed for one parameter defining the dividing surfaces, even for complex, multidimensional reactions. Second, the reaction path can be uniquely defined as the path of steepest descent in a mass-weighted or mass-scaled coordinate system [35, 36], e.g., the minimum energy path (MEP), and this choice of reaction path has further advantages as discussed below. Third, use of a reaction path allows connection to the adiabatic theory of reactions, which provides the basis for including consistent, multidimensional tunneling corrections into VTST.

With this choice of dividing surfaces, a generalized expression for the transition state theory rate constant for a bimolecular reaction is given by:

$$k^{\mathrm{GT}}(T,s) = \sigma\frac{k_{\mathrm{B}}T}{h}\frac{Q^{\mathrm{GT}}(T,s)}{\Phi^{\mathrm{R}}(T)}\exp\left[-\frac{V_{\mathrm{MEP}}(s)}{k_{\mathrm{B}}T}\right] \tag{27.1}$$

where T is temperature, s is the distance along the reaction path with the convention that $s = 0$ at the saddle point and $s < 0$ (> 0) on the reactant (product) side of

the reaction path, σ is a symmetry factor, k_B is Boltzmann's constant, h is Planck's constant, $Q^{GT}(T,s)$ is the generalized transition state partition function for the bound modes orthogonal to the reaction path at s, $\Phi^R(T)$ is the reactant partition function per unit volume and includes the translational partition function per unit volume for the relative motion of the two reacting species, and $V_{MEP}(s)$ is the potential evaluated on the MEP at s. The symmetry factor σ accounts for the fact that the generalized transition state partition function is computed for one reaction path, and for reactions with equivalent reaction paths this partition function needs to be multiplied by the number of equivalent ways the reaction can proceed. In computing the vibrational frequencies that are required to evaluate $Q^{GT}(T,s)$ at a value s of the reaction coordinate, we use a projection operator to project seven degrees of freedom out of the system's Hessian so that the frequencies correspond to a space orthogonal to the reaction coordinate and to three overall translations and three overall vibrations [37–40].

Canonical variational theory (CVT) is obtained by minimizing the generalized transition state rate expression $k^{GT}(T,s)$ with respect to the location s of the dividing surface along the reaction coordinate:

$$k^{CVT}(T) = \min_s k^{GT}(T,s) = k^{GT}\left[T, s^{CVT}(T)\right] \tag{27.2}$$

where $s^{CVT}(T)$ is the location of the dividing surface that minimizes Eq. (27.1) at temperature T.

Sometimes it is convenient to write Eq. (27.1) as [16]

$$k^{GT}(T,s) = \frac{k_B T}{h} K^{\ddagger o} \exp\left[-\Delta G_T^{GT,o}(s) \Big/ RT\right] \tag{27.3}$$

where $K^{\ddagger o}$ is the reciprocal of the standard-state concentration for bimolecular reactions (it is unity for unimolecular reactions), R is the gas constant, and $\Delta G_T^{GT,o}$ is the standard-state generalized-transition-state theory molar free energy of activation. Then Eq. (27.2) becomes

$$k^{CVT}(T) = \frac{k_B T}{h} K^{\ddagger o} \exp\left(-\Delta G_T^{CVT,o} \Big/ RT\right) \tag{27.4}$$

where

$$\Delta G_T^{CVT,o} = \Delta G_T^{GT,o}\left(s^{CVT}\right) \tag{27.5}$$

is the standard-state quasithermodynamic molar free energy of activation at temperature T.

Although we have described the theory in terms of taking the reaction path as the MEP in isoinertial coordinates, this can be generalized to arbitrary paths by methods discussed elsewhere [41]. The treatment of the reaction coordinate at geometries off the reaction path also has a significant effect on the results; one can use either rectilinear [34, 37–39] or curvilinear [40, 42] coordinates for this pur-

pose, where the latter are more physical and more accurate. In particular, the vibrational modes are less coupled in curvilinear coordinates, and therefore anharmonic mode–mode coupling, which is hard to include, is less important. Recently a method has been presented for including anharmonicity in rate constant calculations of general polyatomics using curvilinear coordinates [43].

An expression similar to Eq. (27.1), but for a microcanonical ensemble (fixed energy instead of temperature) can be obtained for the generalized transition-state microcanonical rate constant. Optimizing the location of the dividing surface for this microcanonical expression at each energy and then performing a Boltzmann average of the microcanonical rate constants yields a microcanonical variational theory expression for the temperature-dependent rate constant. Canonical variational theory optimizes the dividing surface for each temperature, whereas microcanonical variational theory optimizes the dividing surface for each energy, and gives a rate constant that is lower than or equal to the CVT one [7, 15]. The improved canonical variational theory (ICVT) [16] is a compromise between CVT and the microcanonical theory, which only locates one optimum dividing surface for each temperature, but removes contributions from energies below the maximum in the ground-state adiabatic potential. The proper treatment of the reaction threshold in the ICVT method recovers most of the differences between the CVT and microcanonical theory. In most cases, CVT and ICVT give essentially the same predicted rate constants.

Equations (27.1) and (27.2) are "hybrid" quantized expressions in which the bound modes orthogonal to the reaction coordinate are treated quantum mechanically, that is, the partition functions $Q^{GT}(T,s)$ and $\Phi^{R}(T)$ are computed quantum mechanically for the bound degrees of freedom, although the reaction coordinate is still classical. In recent work we often use the word "quasiclassical" to refer to this hybrid. Others, mainly organic chemists and enzyme kineticists, often call this "semiclassical," but chemical physicists eschew this usage because "semiclassical" is often a good description for the WKB-like methods that are used to *include* tunneling.

The "hybrid" or "quasiclassical" approach is very old [1]. As the next step we go beyond the standard treatment, and we discuss using the adiabatic theory to develop a procedure for including quantum effects on reaction coordinate motion. A critical feature of this approach is that it is only necessary to make a partial adiabatic approximation, in two respects. First, one needs to assume adiabaticity only locally, not globally. Second, even locally, although one uses an adiabatic effective potential, one does not use the adiabatic approximation for all aspects of the dynamics.

27.2.1
Adiabatic Theory of Reactions

The adiabatic approximation for reaction dynamics assumes that motion along the reaction coordinate is slow compared to the other modes of the system and the latter adjust rapidly to changes in the potential from motion along the reaction coordinate. This approximation is the same as the Born–Oppenheimer electronically adiabatic separation of electronic and nuclear motion, except that here we

use the vibrationally adiabatic approximation for an adiabatic separation of one coordinate, the reaction coordinate, from all other nuclear degrees of freedom [1, 14, 44]. The Born–Oppenheimer approximation is justified based on the large mass difference between electrons and atoms. It is less clear that the adiabatic approximation should be valid for separating different nuclear degrees of freedom, although a general principle for applying this to chemically reactive systems near the dynamical bottleneck would be that near the reaction threshold energy (which is the important energy range for thermally averaged rate constants), the reaction coordinate motion is slow because of the threshold condition. As we discuss below, the vibrationally adiabatic approximation can provide a useful framework for treating quantum mechanical tunneling.

For chemical reactions, the adiabatic approximation is made in a curvilinear coordinate system where the reaction coordinate s measures progress along a curved path through Cartesian coordinates, and the remainder of the coordinates $\mathbf{u}$ are locally orthogonal to this path. Note that the effective mass for motion along the reaction coordinate is unambiguously defined by the transformation from Cartesian to curvilinear coordinates. The effective mass may be further changed by scaling of the coordinates and momenta. When one scales a coordinate u_m by a constant $c^{1/2}$, one must change the reduced mass μ_m for that coordinate by a factor of c^{-1} so that the kinetic energy, $\frac{1}{2}\mu_m\dot{u}_m^2$, where an overdot denotes a time derivative, stays the same [45]. We are free to choose the value of the reduced mass for each coordinate, and we choose it consistently to be the same value μ for all coordinates because this makes it easier to write the kinetic energy for curved paths and for paths at arbitrary orientations with respect to the axes, and it makes it easier to make physical dynamical approximations. Coordinate systems in which the reduced masses for all motions are the same are called isoinertial. In the present article we call the constant reduced mass μ and set it equal to the mass of the hydrogen atom to allow easier comparison of intermediate quantities that depend on the reaction coordinate.

A convenient choice of the reaction path is the MEP in isoinertial coordinates, because by construction the gradient of the potential $V(s,\mathbf{u})$ is tangent to s and there is no coupling between s and $\mathbf{u}$ through second order. Therefore the potential can be conveniently approximated by

$$V(s,\mathbf{u}) = V_{\mathrm{MEP}}(s) + V_{\mathbf{u}}(\mathbf{u};s) \approx V_{\mathrm{MEP}}(s) + \sum_{i,j} u_i H_{ij}(s) u_j \tag{27.6}$$

where the Hessian matrix for a location s along the reaction coordinate is given by

$$H_{ij}(s) = \left.\frac{\partial^2 V}{\partial u_i \partial u_j}\right|_{s,u_i=u_j=0} \tag{27.7}$$

and we choose the origin for the $\mathbf{u}$ coordinates to be on the MEP. Although the potential energy term in these coordinates is simple, the kinetic energy term is complicated by factors dependent upon the curvature of the reaction path [13, 14,

37, 46]. As a first approximation we will assume that the reaction-path curvature can be neglected, but we will eliminate this approximation after Eq. (27.22) because the curvature of the reaction path is very important for tunneling.

Treating bound modes quantum mechanically, the adiabatic separation between s and $\mathbf{u}$ is equivalent to assuming that quantum states in bound modes orthogonal to s do not change throughout the reaction (as s progresses from reactants to products). The reaction dynamics is then described by motion on a one-mathematical-dimensional vibrationally and rotationally adiabatic potential

$$V_a(\mathbf{n}, \Lambda, s) = V_{MEP}(s) + \varepsilon_{int}^{GT}(\mathbf{n}, \Lambda, s) \tag{27.8}$$

where $\mathbf{n}$ and Λ are quantum numbers for vibrations and rotations, respectively, and $\varepsilon_{int}^{GT}(n, \Lambda, s)$ is the vibrational-rotational energy of quantum state $(\mathbf{n},\Lambda)$ of the generalized transition state at s. In a rigid-body, harmonic approximation, the generalized transitive-state energy level is given by

$$\varepsilon_{int}^{GT}(\mathbf{n}, \Lambda, s) = \sum_m \hbar\omega_m(s)\left(n_m + \frac{1}{2}\right) + \varepsilon_{rot}^{GT}(\Lambda, s) \tag{27.9}$$

where the harmonic vibrational frequencies $\omega_m(s)$ are obtained from the nonzero eigenvalues of the Hessian matrix in Eq. (27.7), and the rotational energy level $\varepsilon_{rot}^{GT}(\Lambda, s)$ is determined for the rigid-body geometry of the MEP at location s. Six of the eigenvalues of the Hessian will be zero (for a nonlinear system), corresponding to three rotations and three translations of the total system.

If the reaction coordinate is treated classically, the probability for reaction on a state $(\mathbf{n},\Lambda)$ at a total energy E is zero if the energy is below the maximum in the adiabatic potential for that state, and 1 otherwise:

$$P_C^A(\mathbf{n}, \Lambda, E) = \theta\left[E - V_a^A(\mathbf{n}, \Lambda)\right] \tag{27.10}$$

where $V_a^A(\mathbf{n}, \Lambda)$ is the absolute maximum of the adiabatic potential $V_a(\mathbf{n}, \Lambda, s)$ and $\theta(x)$ is a Heaviside step function such that $\theta(x) = 0$ (1) for $x < 0$ (> 0). Since the classical reaction probability is determined entirely by whether the energy is above the adiabatic barrier or not, the neglect of reaction-path curvature in the kinetic energy term does not matter. We shall see below that this is not true when the reaction path is treated quantum mechanically, in which case the curvature of the reaction path must be included.

An expression for the rate constant can be obtained by the proper Boltzmann average over total energy E and sum over vibrational and rotational states

$$k^A(T) = \left[h\Phi^R(T)\right]^{-1} \int dE \exp(-E/k_B T) \sum_{\mathbf{n},\Lambda} P_C^A(\mathbf{n}, \Lambda, E) \tag{27.11}$$

which can be reduced for a bimolecular reaction to

$$k^A(T) = \frac{k_B T}{h\Phi^R(T)} \sum_{\mathbf{n},\Lambda} \exp\left[-V_a^A(\mathbf{n}, \Lambda)/k_B T\right] \tag{27.12}$$

Like Eq. (27.2), Eqs. (27.11) and (27.12) are also hybrid quantized expressions in which the bound modes are treated quantum mechanically but the reaction coordinate motion is treated classically. Whereas it is difficult to see how quantum mechanical effects on reaction coordinate motion can be included in VTST, the path forward is straightforward in the adiabatic theory, since the one-dimensional scattering problem can be treated quantum mechanically. Since Eq. (27.12) is equivalent to the expression for the rate constant obtained from microcanonical variational theory [7, 15], the quantum correction factor obtained for the adiabatic theory of reactions can also be used in VTST.

27.2.2 Quantum Mechanical Effects on Reaction Coordinate Motion

A fully quantum mechanical expression for the rate constant within the adiabatic approximation is given by replacing the classical reaction probabilities in Eq. (27.11) with quantum mechanical ones $P_Q^A(\mathbf{n}, \Lambda, E)$ corresponding to one-dimensional transmission through the potential $V_a(\mathbf{n},\Lambda,s)$. Note that, at the energies of interest, tunneling and nonclassical reflection by this potential are controlled mainly by its shape near the barrier top, that is, near the variational transition state. Thus $P_Q^A(\mathbf{n}, \Lambda, s)$ only requires the assumption of local vibrational adiabaticity along with the observation that reactive systems pass through the dynamical bottleneck region in quantized transition states [47]. The quantum mechanical vibrationally and rotationally adiabatic rate constant can be expressed in terms of the hybrid expression in Eq. (27.12) by

$$k^{VA}(T) = \kappa^{VA}(T)\, k^A(T) \tag{27.13}$$

where the transmission coefficient is defined by

$$\kappa^{VA}(T) = \frac{\int_0^\infty dE \exp(-E/k_B T) \sum_{\mathbf{n},\Lambda} P_Q^A(\mathbf{n}, \Lambda, E)}{\int_0^\infty dE \exp(-E/k_B T) \sum_{\mathbf{n},\Lambda} P_C^A(\mathbf{n}, \Lambda, E)} \tag{27.14}$$

Rather than compute the reaction probabilities for all quantum states that contribute significantly to the sum in Eq. (27.14), we approximate the probabilities for all excited states by the probabilities for the ground state with the energy shifted by the difference in adiabatic barrier heights (relative to a single overall zero of energy) for the excited state, $V_a^A(\mathbf{n}, \Lambda)$, and ground state, V_a^{AG} [16]:

$$P_Q^A(\mathbf{n}, \Lambda, E) = P_Q^{AG}\left[E - V_a^A(\mathbf{n}, \Lambda) - V_a^{AG}\right] \tag{27.15}$$

where $P_Q^{AG}(E)$ is the reaction probability for the ground-state adiabatic potential. This approximation assumes that adiabatic potentials for excited states are similar in shape to the ground-state potential. Although this approximation is not valid in

general, it works surprisingly well for calculating the transmission coefficient because at low temperatures the transmission coefficient is dominated by contributions from the ground state or states energetically similar to the ground state, and at high temperatures, where classical mechanics becomes valid, it correctly goes to a value of one. With this approximation the transmission coefficient takes the form

$$\kappa^{\mathrm{VAG}}(T) = \frac{\int_0^\infty \mathrm{d}E\, \exp(-E/k_{\mathrm{B}}T) P_{\mathrm{Q}}^{\mathrm{AG}}(E)}{\int_0^\infty \mathrm{d}E\, \exp(-E/k_{\mathrm{B}}T) P_{\mathrm{C}}^{\mathrm{AG}}(E)} \tag{27.16}$$

where G in general denotes the ground state, $P_{\mathrm{Q}}^{\mathrm{AG}}(E)$ is $P_{\mathrm{Q}}^{\mathrm{A}}(\mathbf{n}, \Lambda, E)$ with $\mathbf{n}$, Λ in the ground state, and $P_{\mathrm{C}}^{\mathrm{AG}}(E)$ is like $P_{\mathrm{Q}}^{\mathrm{AG}}(E)$ for all degrees of freedom except the reaction coordinate, but with the reaction coordinate motion classical. Then

$$P_{\mathrm{C}}^{\mathrm{AG}}(E) = \theta\left(E - V_{\mathrm{a}}^{\mathrm{AG}}\right) \tag{27.17}$$

where

$$V_{\mathrm{a}}^{\mathrm{AG}} = V_{\mathrm{a}}^{\mathrm{A}}[(\mathbf{n}, \Lambda) = G] \tag{27.18}$$

This yields

$$\kappa^{\mathrm{VAG}}(T) = (k_{\mathrm{B}}T)^{-1} \exp\left(V^{\mathrm{AG}}/k_{\mathrm{B}}T\right) \int_0^\infty \mathrm{d}E \exp(-E/k_{\mathrm{B}}T) P_{\mathrm{Q}}^{\mathrm{AG}}(E) \tag{27.19}$$

We first consider the case where the reaction probabilities are computed for the adiabatic model with the reaction-path curvature neglected, the so-called vibrationally adiabatic zero-curvature approximation [36]. We approximate the quantum mechanical ground-state probabilities $P_{\mathrm{Q}}^{\mathrm{AG}}(E)$ for the one-dimensional scattering problem by a uniform semiclassical expression [48], which for $E < V^{\mathrm{AG}}$ is given by

$$P^{\mathrm{SAG}}(E) = \{1 + \exp[2\theta(E)]\}^{-1} \tag{27.20}$$

where the imaginary action integral is

$$\theta(E) = \hbar^{-1} \int_{s_<}^{s_>} \mathrm{d}s \left\{2\mu\left[V_{\mathrm{a}}^{\mathrm{G}}(s) - E\right]\right\}^{\frac{1}{2}} \tag{27.21}$$

μ is the mass for motion along the reaction coordinate, $V_{\mathrm{a}}^{\mathrm{G}}(s)$ is the ground-state adiabatic potential, that is $V_{\mathrm{a}}(\mathbf{n}, \Lambda, s)$ for $\mathbf{n} = \Lambda = 0$, and $s_<$ and $s_>$ are the classical turning points, that is the locations where $V_{\mathrm{a}}^{\mathrm{G}}(s) = E$. The uniform semiclassical

approximation can be extended to energies above the ground-state barrier maximum for a parabolic barrier [48]

$$P^{SAG}(V^{AG} + \Delta E) = 1 - P^{SAG}(V^{AG} - \Delta E) \tag{27.22}$$

and we use this method to obtain reaction probabilities for energies above the barrier maximum up to $2V^{AG} - E_0$, where E_0 is the maximum of the reactant and product zero-point energies. For higher energies the probability is set to one.

When one uses CVT, one must replace $P_C^{AG}(E)$ by an approximation that is consistent with the threshold implicitly assumed by CVT. In particular we replace V_a^{AG} by $V_a^G[s^{CVT}(T)]$ in Eq. (27.17). This then yields for the rate constant with tunneling

$$k^{CVT/MT}(T) = \kappa(T)k^{CVT}(T) \tag{27.23}$$

where

$$\kappa(T) = \frac{\int_0^\infty d(E/k_B T)\exp(-E/k_B T)P_Q^{AG}}{\exp\{-V_a^G[s^{CVT}(T)]\}} \tag{27.24}$$

and where MT can be SCT, LCT, or OMT.

The inability of the zero-curvature tunneling (ZCT) approximation to provide reliable rate constants has been known for over 30 years [10, 36], and over the last 25 years significant progress has been made in developing approaches to treat the multidimensional effect of reaction-path curvature in adiabatic calculations of reaction probabilities. The most successful methods for including the multidimensional effect of reaction-path curvature in adiabatic calculations of reaction probabilities specify a tunneling path that 'cuts the corner' and shortens the tunneling length [18]. Marcus and Coltrin [25] found the optimum tunneling path for the collinear H + H_2 reaction by finding the path that gave the least exponential damping. General multidimensional tunneling (MT) methods, applicable to polyatomic reactions, have been developed that are appropriate for systems with both small [17, 18, 22, 24] and large [20, 23, 34] reaction path curvature, as well as more general methods that optimize tunneling paths by a least-imaginary-action principle [20, 39]. In practice it is usually sufficient to optimize the imaginary action from among a small set of choices by choosing either the small-curvature tunneling (SCT) approximation or the large-curvature tunneling (LCT) approximation, whichever gives more tunneling at a given tunneling energy; this is called microcanonical optimized multidimensional tunneling (μOMT), or, for short, optimized multidimensional tunneling (OMT) [23, 49]. These methods are discussed below in more detail in the context of illustrative examples of H-transfer processes, but we anticipate that discussion and the later discussion of con-

densed-phase reactions by noting that all MT approximations generalize Eq. (27.24) to

$$\kappa(T) = \frac{\int_0^\infty d(E/k_B T)\exp(-E/k_B T)P(V_1, V_2|E)}{\exp\{-V_2[s_*(T)]/k_B T\}} \tag{27.25}$$

where V_1 is the effective multidimensional potential energy surface, V_2 is the effective one-dimensional adiabatic potential energy curve, and $s_*(T)$ is the variational transition state location at temperature T. In the ZCT and SCT approximations, one need not specify V_1, that is the tunneling depends only on the effective one-dimensional adiabatic potential energy curve, but in the LCT and OMT approximations we need to know more about the potential energy surface than just the information contained in $V_2(s)$. For gas-phase reactions, $V_2(s)$ is just $V_a^G(s)$, and V_1 is the full potential energy surface.

27.3
H-atom Transfer in Bimolecular Gas-phase Reactions

Gas-phase reactions of two interacting reactants have provided a fertile ground for developing and testing methods for treating H-transfer reactions. In particular, triatomic reactions like H + H_2 have been instrumental in this development and in helping us understand the limits of validity of the approximations used in these methods, because accurate quantum mechanical results are available for comparison. We present three examples of reactions that help us present details of the methods as well as features displayed by H-atom transfers.

27.3.1
H + H_2 and Mu + H_2

The H + H_2 reaction and its isotopic variants have been extensively studied over the years. Muonium (Mu) is one of the most interesting isotopes studied for this reaction because Mu (consisting of a positive muon and an electron) has a mass that is about 8.8 times smaller than that of H and has the potential to exhibit very large kinetic isotope effects. Even though both reactions, H + H_2 and Mu + H_2, involve the transfer of a H atom, the presence of the much lighter Mu atom drastically changes the nature of the quantum mechanical effects on the H-transfer process. Calculations of H- and Mu-transfer rate constants are illustrated here using the Liu–Siegbahn–Truhlar–Horowitz (LSTH) potential energy surface [50].

The traditional treatment of KIEs is based upon conventional TST [29, 30], in which the dividing surface is placed at the saddle point of the reaction, with tunneling effects generally included by a separable approximation such as the Wigner

correction or Bell parabolic tunneling. Using this approach with the harmonic approximation, the Mu/H KIE is determined by

$$\frac{k_{Mu}}{k_H} = \frac{\kappa^W_{Mu}}{\kappa^W_H} \frac{\Phi^R_H}{\Phi^R_{Mu}} \frac{Q_{Mu}}{Q_H} \tag{27.26}$$

The Wigner correction for tunneling depends only on the imaginary frequency $\omega_{s,X}$ for the unbound mode at the saddle point [8]

$$\kappa_X = 1 + \frac{1}{24}\left(\frac{\hbar|\omega_{s,X}|}{k_B T}\right)^2 \tag{27.27}$$

Reactant vibrational and rotational partition functions are the same for both reactions (i.e., those for H_2) and the ratio of reactant partition functions reduces to the ratio of translational partition functions, which depends only on the reduced masses for the relative motion of the reactants

$$\frac{\Phi^R_H}{\Phi^R_{Mu}} = \left[\frac{m_H(m_{Mu} + 2m_H)}{m_{Mu}(3m_H)}\right]^{\frac{3}{2}} \approx 15.5 \tag{27.28}$$

The ratio of partition functions for bound modes at the saddle point is determined by the frequencies for those modes,

$$\frac{Q_{Mu}}{Q_H} = \prod_{i=1}^{F-1} \frac{\sinh\left(\hbar\omega_{Mu,i}/2k_B T\right)}{\sinh\left(\hbar\omega_{H,i}/2k_B T\right)} \tag{27.29}$$

where F is the number of vibrational modes. With the rate constant for the reaction with the light mass in the numerator, a KIE is termed 'normal' if it is greater than one. Because of the large difference in masses, the saddle point frequencies for the Mu reaction are larger than those of the H reaction, and the ratio of saddle point partition functions is less than one. The imaginary frequency for the reaction coordinate motion is also higher for the Mu reaction than for the H reaction, so that the ratio of tunneling factors is greater than one as well as the ratio of reactant partition functions. The saddle point frequencies for these two reactions using the LSTH potential energy surface are (2059, 909, and 1506 i cm^{-1}) and (4338, 1382, and 1784 i cm^{-1}) and for the (stretch, bend, and unbound) modes for $H + H_2$ and $Mu + H_2$, respectively. Using these frequencies in harmonic transition state theory with Wigner tunneling gives a KIE less than one, which is termed inverse, as shown in Fig. 27.1, where the TST/W results are compared with experiment [51]. Although TST with Wigner tunneling gives the right qualitative trend, both the magnitude and slope are inaccurate. We next discuss the other curves in Fig. 27.1, which present improvements in the treatment of quantum mechanical effects for the hydrogen transfer process.

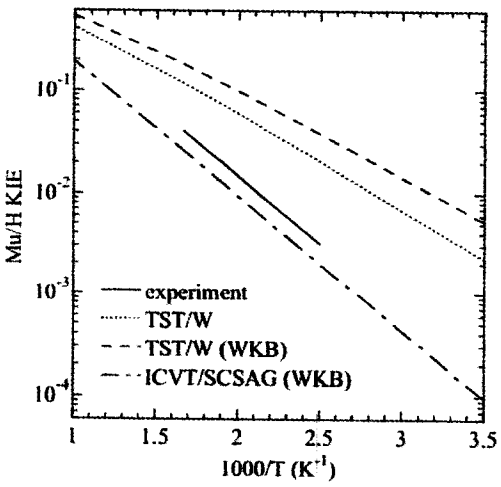

Figure 27.1 Kinetic isotope effects for the Mu/H + H_2 reaction as a function of temperature.

A first consideration is the treatment of the bound vibrational modes, which in the TST/W results shown in Fig. 27.1, use the harmonic approximation. The total harmonic zero-point energy at the saddle point (for stretch and bend vibrations) is much higher for the Mu reaction, 10.2 kcal mol^{-1}, than for the H reaction, 5.5 kcal mol^{-1}. As shown in Fig. 27.2, the stretching vibration extends to larger distances and higher energies for the Mu reaction than for the H reaction, and therefore accesses more anharmonic parts of the potential. In this situation methods for including anharmonicity must be considered [52, 53].

The straight lines through the saddle point end at the classical turning points for the harmonic approximation to the stretch potential at the saddle point. For the symmetric H + H_2 reaction the harmonic turning points extend just past the 12 kcal mol^{-1} contour, and on the concave side, it is very close to the accurate anharmonic turning point, calculated using a WKB approximation [53]. For the Mu + H_2 reaction the harmonic turning point on the concave side falls short of the anharmonic turning point, which is near the 16 kcal mol^{-1} contour, and it extends past the 20 kcal mol^{-1} contour on the convex side of the turning point, clearly indicating that the potential for this mode is quite anharmonic. Comparison of the curves label TST/W (harmonic treatment) and TST/W (WKB) in Fig. 27.1 shows the importance of anharmonicity in the quantum treatment of bound states. When the vibrational modes at the saddle point are treated more accurately using a WKB method [53], the Mu rate constants are increased by about a factor of two, while the H rate constants change only slightly, leading to a larger disagreement with experiment for the KIE.

A more accurate treatment of the reaction uses variational TST, in which the dividing surface is allowed to move off the saddle point, or equivalently, uses the adiabatic theory as described in Section 27.2. The vibrationally adiabatic potential

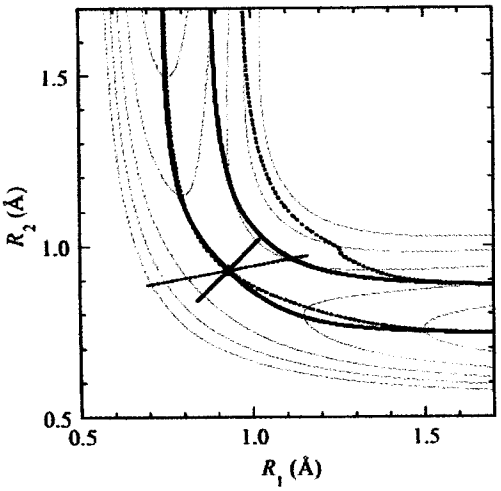

Figure 27.2 Potential energy contours (thin solid curves) at 4, 8, 12, 16, and 20 kcal mol^{-1} are shown for collinear A–HH geometries (A = H or Mu) with HH and AH distances represented by R_1 and R_2, respectively. The solid diamond denotes the saddle point. Thick solid and dashed curves are for the H and Mu reactions, respectively. Harmonic stretch vibrational modes are the straight lines through the saddle point. Minimum energy paths are the curved lines through the saddle point. The curved lines on the concave side of the MEP are paths of turning points for the anharmonic stretch vibration.

curves for the two reactions are shown in Fig. 27.3 and are compared with the potential along the MEP. The MEPs for the two reactions, as shown in Fig. 27.2, are very close to each other, so that the potentials along the MEP are also about the same. Note that the MEPs are paths of steepest descent in a mass-weighted or mass-scaled coordinated system, and therefore, the MEPs for the H and Mu reactions are slightly different. The largest differences are seen in the entrance channel (large R_1) where the reaction coordinate is dominated by either H or Mu motion relative to H_2, while in the exit channel (large R_2) the reaction coordinate for both reactions is an H atom moving relative to the diatomic product (either H_2 or MuH). The reaction coordinate in Fig. 27.3 is defined as the arc length along the MEP through mass-weighted coordinates. To facilitate comparisons of potential curves for the two reactions, we use the same effective mass for the mass weighting – the mass of the hydrogen atom. Because the mass of Mu is so much lighter than H, the scale of s on the reactant side is contracted when the same mass weighting is used for both reactions, leading to a steeper increase for Mu.

The ground-state adiabatic potential curves in Fig. 27.3 are constructed by adding accurate anharmonic zero-point energies for the stretch and bend modes to V_{MEP}. On the reactant side the shapes of V_{MEP} and V_a^G are very similar with the adiabatic potential being shifted up by approximately the zero-point energy for the H_2 stretch vibrations, 6.2 kcal mol^{-1}. Near the saddle point this contribution decreases markedly for the H + H_2 reaction, to 2.9 kcal mol^{-1}, causing the adia-

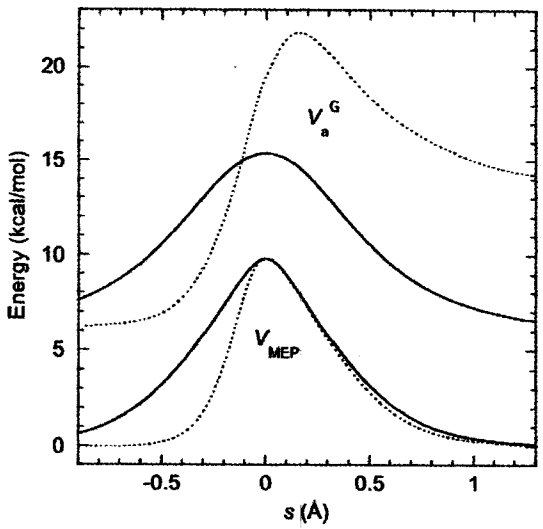

Figure 27.3 Potential along the MEP (V_{MEP}, lower pair of curves) and ground-state adiabatic potential (V_a^G, upper pair of curves) as a function of reaction coordinate s for the H + H_2 reaction (solid lines) and Mu + H_2 reaction (dashed line).

batic potential to be less peaked than V_{MEP} for this reaction. Contributions from the bending vibration near the saddle point are about 2.6 kcal mol^{-1}, otherwise the adiabatic potential curve would be even flatter near the saddle point. The zero-point energy for MuH is 13.4 kcal mol^{-1}, which accounts for the large difference in the H and Mu adiabatic curves in the product region and the shift of its maximum toward products. The difference in the maximum of the adiabatic curve and its value at the saddle point is about 2.3 kcal mol^{-1}, which leads to a decrease by about a factor of 10 in the Mu rate constant at 500 K. This is the main reason for the large shift in the curve labeled ICVT/SCSAG (WKB) relative to the TST/W (WKB) curve in Fig. 27.1.

We now turn our attention to the issue of quantum mechanical tunneling in these H-atom transfer reactions. The Wigner and Bell tunneling methods use the shape of V_{MEP} at the saddle point to estimate the tunneling correction. The effective mass for the reaction coordinate in Fig. 27.3 is the same for both reactions, therefore, tunneling is treated as the motion of a particle with the mass of a hydrogen atom through the potentials in the figure. The similarity in the V_{MEP} curves for H and Mu indicates why the tunneling correction using these methods gives similar results for the H and Mu reactions. For example, Wigner tunneling gives corrections for Mu that are less than 30% higher those for H for 300 K and higher temperatures. The shapes of the adiabatic curves exhibit greater differences with the curve for the Mu reaction having a narrow barrier near the maximum. When reaction-path curvature is neglected, the tunneling correction factors for Mu are factors of 2.5 and 1.6 higher than those for H at temperatures of 300 and 400 K.

As discussed above, the most accurate methods for treating tunneling include the effects of reaction-path curvature. The original small-curvature tunneling (SCT) method [17] provides an accurate description of the H-transfer process in these triatomic H-atom transfer reactions. In the Marcus–Coltrin method [25] the tunneling occurs along the path of concave-side turning points for the stretch vibration orthogonal to the reaction coordinate. Figure 27.2 shows paths of turning points $t_{str}(s)$ for the stretch vibration for the H/Mu + H_2 reactions, where the turning points are obtained for the anharmonic potential at the WKB zero-point energy. Tunneling along this path shortens the tunneling distance and the effect of the shortening of the path can be included in the calculation of the action integral by replacing the arc length along the MEP ds in Eq. (27.15) by the arc length along this new path $d\xi$, or equivalently by including the Jacobian $d\xi/ds$ in the integrand of Eq. (27.15). An approximate expression for $d\xi/ds$ can be written in terms of the curvature of the MEP and vibrational turning points [17, 18]. The MEP is collinear for the H + H_2 reaction and the curvature coupling the bend vibration to the reaction coordinate is zero for collinear symmetry. Therefore, the Jacobian can be written just in terms of the one mode

$$\left(\frac{d\xi}{ds}\right)^2 \approx [1 - \kappa(s)t_{str}(s)]^2 + \left(\frac{dt_{str}}{ds}\right)^2 \tag{27.30}$$

The SCT method extends the Marcus–Coltrin idea in a way that eliminates problems with the Jacobian becoming unphysical. Rather than including the Jacobian factor, the reduced mass for motion along the reaction coordinate μ is replaced by $\mu_{eff}(s)$ in Eq. (27.21), where $\mu_{eff}(s)$ is given by

$$\frac{\mu_{eff}(s)}{\mu} \approx \min\left\{1, \exp\left[-2a(s) - [a(s)]^2 + \left(\frac{dt_{str}}{ds}\right)^2\right]\right\} \tag{27.31}$$

$$a(s) = \kappa(s)t_{str}(s) \tag{27.32}$$

where $\kappa(s)$ is the curvature coupling between the reaction coordinate motion and the stretch vibrational motion [37]. Note that the signs of $\kappa(s)$ and $t_{str}(s)$ are chosen so that the path lies on the concave side of the path and their product $a(s)$ is positive.

The reaction-path curvature is given by the coupling of the stretch vibration to the reaction coordinate in the mass-weighted coordinate system, not the coordinate system used to display the paths in Fig. 27.2. The reaction Mu + H_2 has smaller reaction-path curvature than the H + H_2 reaction, by about a factor of two in the region near the peak of the adiabatic barriers, and the enhancement of the tunneling from corner cutting is much less for the Mu reaction. Neglect of reaction-path curvature gave tunneling factors for the Mu reaction that are much higher than those for the H reaction and including the effects of the curvature greatly reduces this large difference. In fact, at 300 K without curvature the Mu reaction

has a tunneling factor that is 2.5 times larger than the H reaction and this is reduced to an enhancement of only 2% when curvature is included with the SCT method. For temperatures from 400 to 600 K, the SCT tunneling factors for the Mu reaction are lower than those for the H reaction by about 9%. When these effects are included the predicted KIEs are in good agreement with the experimental results, being only 30–40% low, as shown in Fig. 27.1.

The H/Mu + H_2 reactions are examples of H-atom transfers with relatively small reaction-path curvature and provide a good example of how the description of the hydrogen transfer process is effected by quantization of bound modes, variational optimization of the location of the dividing surface, and inclusion of quantum mechanical effects on reaction coordinate motion. The magnitude of the reaction-path curvature for an H-atom transfer reaction is often correlated with the skew angle, where the skew angle is defined as the angle between the gradient along the reaction path in the product channel with that in the reactant channel. For the H-atom transfer reaction AH + B → A + BH this angle is defined by

$$\cos\,\beta_{\text{skew}} = \left[\frac{m_A m_B}{(m_A + m_H)(m_B + m_H)}\right]^{1/2} \tag{27.33}$$

where A and B can be atomic or polyatomic moieties with masses m_A and m_B. Skew angles for the H and Mu reactions are 60° and 77°, respectively, and we saw above how the larger curvature in the system with the smaller skew-angle system resulted in greater tunneling. When the masses of A and B are much larger than the mass of H, the skew angle can become very small, resulting in large reaction-path curvature. These systems require tunneling methods that go beyond the small-curvature approach used here.

27.3.2
Cl + HBr

The collinear Cl + HBr reaction provides an example of a system with a very small skew angle. Figure 27.4 shows potential energy contours for this collinear reaction in mass-scaled coordinates x and y for the potential energy surface of Babamov et al. [54], where x is the distance from Cl to the center of mass of HBr and y is a scaled HBr distance. The kinetic energy is diagonal in this coordinate system and the scaling of y is chosen so that the effective masses for x and y motion are the same. Therefore, reaction dynamics in this coordinate system can be viewed as a single mass point moving on the potential energy contours in Fig. 27.4. The skew angle, which in this coordinate system is the angle between the minimum energy path in the asymptotic reactant channel and the asymptotic product channel, is only 12°. Regions of large reaction-path curvature, which can be seen near the saddle point, lead to a breakdown of the approximations used in the SCSAG method. The approximation of vibrational adiabaticity is valid in the entrance and exit channels where the stretch vibration is dominated by motion of the hydrogen

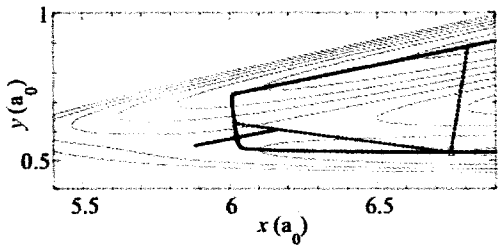

Figure 27.4 Potential energy contours (thin solid curves) from −10 to 20 kcal mol^{-1} (spaced every 5 kcal mol^{-1}) are shown for the collinear Cl–H–Br reaction as a function of internal coordinates x and y (see text). A solid diamond denotes the saddle point and the thick straight line through the saddle point is the anharmonic vibrational mode. The thick solid curve is the minimum energy path. The classical turning point on the ground-state adiabatic potential energy curve at 9 kcal mol^{-1} is indicated by the unfilled symbol in the entrance channel. Turning points for adiabatic potential curves with the stretch vibration in its ground state ($n = 0$) and excited state ($n = 2$) are shown as an unfilled circle ($n = 0$) and square ($n = 2$) in the exit channel. Dashed lines connect the turning point for the ground-state adiabatic potential curve in the entrance channel with the turning points for $n = 0$ and 2 in the exit channel.

atom. At the saddle point the vibrational motion more nearly resembles the relative motion of the two heavy atoms leading to a low vibrational energy (e.g., only 0.4 kcal mol^{-1} at the saddle point compared to 3.8 kcal mol^{-1} for reactants). The thick straight line through the saddle point shows the extent of the vibrational motion. Because of the large reaction-path curvature, the regions of vibrational motion in the reactant valley on the concave side of the MEP, just before the bend in the MEP, overlap with the vibrational motion at the saddle point. This complication, and the strong coupling of the reaction coordinate motion to the vibration orthogonal to it, argues against an adiabatic treatment of hydrogen atom tunneling in the saddle point region. For this type of system the LCT method is more appropriate [19, 20, 22, 39, 49, 55], and we describe it briefly here. A key aspect of LCT methods is that the tunneling depends on more aspects of the potential energy surface than just $V_a^G(s)$, and that is why we introduced the multidimensional potential energy surface in Eq. (27.25).

In the vibrationally adiabatic approximation, tunneling at a fixed total energy is promoted by motion along the reaction coordinate and initiates from the classical turning point on the adiabatic potential. The physical picture in the LCT method is that the rapid vibration of the hydrogen atom promotes transfer of the hydrogen atom between the reactant and product valleys and this hopping begins from turning points in the vibrational coordinate on the concave side of the MEP. For a given total energy, tunneling can take place all along the entrance channel, up to the adiabatic turning point, as the reactants approach and recede. Tunneling is assumed to occur along straight-line paths from the reactant to product valleys, subject to the constraint that adiabatic energies in the reactant and product channels are the same. Figure 27.4 illustrates the LCT tunneling paths, where the straight dashed line is the tunneling path connecting points, denoted by open cir-

cles, along the MEP for which the ground-state adiabatic potential curve has an energy of 9 kcal mol^{-1}. In the large-curvature ground state approximation, version 3 or version 4 [22, 39, 49], the straight-line path used to specify a given tunneling path initiates and terminates on the MEP rather than at the turning points for the vibrational motion. This assumption simplifies the extension of the method to polyatomic reactions, and it yields results that are similar to earlier versions of the method with more complicated specifications. In current work one should always use the latest version (version 4) of the LCT method because it incorporates our most complete experience on how to embed the physical approximations in a stable algorithm, although the differences between the versions are small in most cases.

Although the LCT method does not rely on the adiabatic approximation in the region where it breaks down (i.e., the nonadiabatic region), it does use the approximation in the reactant and product channels to determine the termini for the straight-line tunneling paths. Figure 27.5 shows adiabatic potential curves in the reactant and product regions and the potential along the MEP. This reaction is exoergic by about 16 kcal mol^{-1} with a barrier over 10 kcal mol^{-1} higher than the minimum of the reactant valley. Because of the large exoergicity and rapid decrease of the potential along the MEP on the product side, the value of the

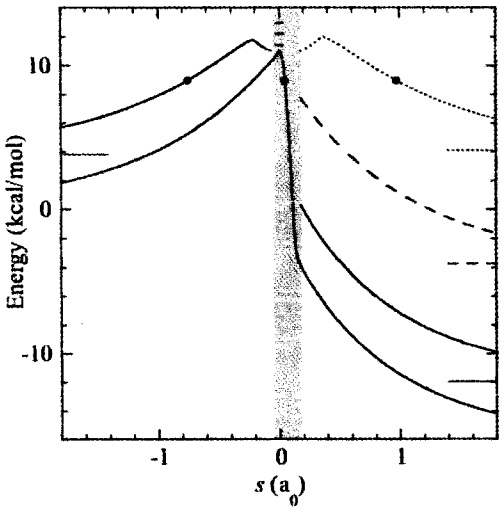

Figure 27.5 Potential along the minimum energy path (lowest continuous curve) and adiabatic potential segments in the reactant and product regions for $n = 0$ (solid curve), 1 (long dashed curve) and 2 (short dashed curve) as a function of reaction coordinate for the collinear Cl + HBr reactions. The values of the adiabatic potential curves in the asymptotic reactant and product regions are shown as short straight-line segments on the left and right of the plot. The gray shaded area around the saddle point is a region where the adiabatic approximation is not valid (see text). The 3 small tick marks at $s = 0$ are the values the 3 adiabatic potential curves would have at the saddle point. The bullets are turning points for a total energy of 9 kcal mol^{-1}.

ground-state adiabatic potential at the edge of the nonadiabatic region on the product side is already quite low (near 0).

The vibrationally adiabatic approximation requires that vibrational quantum numbers remain constant throughout a reaction. The strong coupling induced by the reaction-path curvature can lead to appreciable nonadiabaticity and population of excited states in the product channel, and this effect is included in the LCT method. (As mentioned above, the SCT approximation does not imply global vibrational adiabaticity either, but it does assume adiabaticity for the effective potential during the entire tunneling event itself; the LCT approximation includes vibrational nonadiabaticity even for the effective potential during the tunneling event.) Figure 27.5 shows the product-channel segments of the adiabatic potential curves for the ground and first two excited states. The product-side turning point for the first excited adiabatic curve also falls within the nonadiabatic region like the ground-state one, and on the scale of the plot is not discernible from the ground-state turning point. The energies of the $n = 2$ adiabatic curve are sufficiently high that the turning points occur well out into the product region (around $s = 1$ a_0 for a tunneling energy of 9 kcal mol^{-1}). Figure 27.4 shows the tunneling path corresponding to these turning points. This path is seen to cut the corner significantly. The barrier to tunneling along this path is comparable to the adiabatic barrier and the shorter tunneling path offered by this corner cutting greatly enhances the tunneling. The LCT method was extended to account for contributions from tunneling into excited states of products [55], and for this reaction, the contribution to the tunneling correction factor is dominated by tunneling into the $n = 2$ state.

The small-curvature (SC) and large-curvature (LC) methods were developed to treat tunneling in the cases of two extremes of reaction-path curvature. In the SC methods, the effective tunneling path (which is implicit but never constructed and not completely specified, since it need not be) is at or near the path of concave-side turning points for the bound vibrational motions that are coupled to the reaction coordinate motion. In the LC methods, the effective tunneling paths (which are explicit) are straight-line paths between the reactant and product valleys. The optimum tunneling paths for reactions with intermediate reaction-path curvature may be between these two extremes, and for these reactions the least-action tunneling (LAT) method [20, 39, 56] is most appropriate. In the LAT method, we consider a sequence of tunneling paths depending on a single parameter α such that for $\alpha = 0$ the tunneling path is the MEP and for $\alpha = 1$ it is the LCT tunneling path. The optimum value of α (yielding the optimum tunneling path) for each tunneling energy is determined to minimize the imaginary-action integral and thereby maximize the tunneling probability. Figure 27.6 compares rate constants computed by the ICVT method, including tunneling by SCT, LCT, and LAT methods, with accurate quantum mechanical ones [55] for the collinear Cl + HBr reaction. The adiabatic method (SCT) cannot account for the large probability of populating the $n = 2$ excited product state and underestimates the accurate rate constants by factors of 3 to 6 for temperatures from 200 to 300 K. The LCT and LAT methods agree to within plotting accuracy, and are therefore shown as one

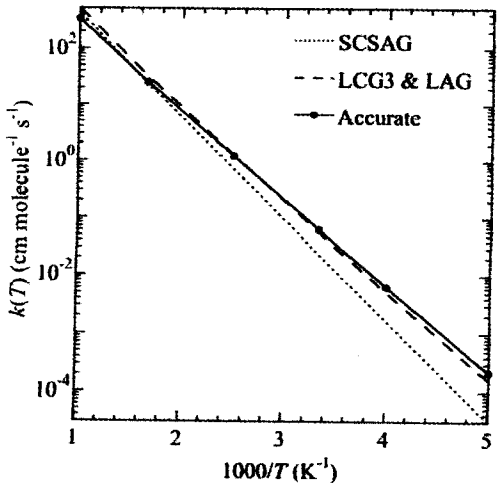

Figure 27.6 Rate constants as a function of temperature for the collinear Cl + HBr reaction. Accurate quantum mechanical rate constants (solid line with bullets) are compared with those computed using improved canonical variational theory (ICVT) with tunneling included by SCSAG (dotted line) and LCG3 and LAG (long dashed line).

curve, indicating that the optimum tunneling paths for this reaction are the straight-line paths connecting the reactant and product valleys. These methods underestimate the accurate rate constants by only 10–25% for T from 200 to 300 K and agree to within 50% over the entire temperature range from 200 to 1000 K. The excellent agreement with accurate rate constants for this model system indicates the good accuracy provided by the LCT and LAT methods for this type of small skew angle reaction.

The physical picture of tunneling in this system provided by the approximate, yet accurate, tunneling methods is very different than descriptions of tunneling in simpler conventional models of tunneling. In the Wigner and Bell tunneling approximations, properties of the potential near the saddle point determine the tunneling correction factors. As illustrated in Fig. 27.4, barriers along straight-line paths, which connect the reactant and product channels, control the actual tunneling in this small-skew angle system, and these paths are significantly displaced from the saddle point.

27.3.3 Cl + CH_4

The higher dimensionality of polyatomic reactions makes them more of a challenge to treat theoretically. Variational transition state theory with multidimensional tunneling has been developed to allow calculations for a wide variety of polyatomic systems. In this section we consider issues that arise when treating polyatomic systems. The Cl + CH_4 reaction provides a good system for this pur-

pose because the accurate SPES potential energy surface of Corchado et al. [57] is available and a variety of experimental results [58] exist to validate the methods.

Hydrogen transfer between Cl and CH_3 corresponds to a heavy–light–heavy mass combination and this reaction has a small skew angle of about 17° and regions of large curvature along the reaction path. The reaction is endoergic by 6.1 kcal mol^{-1} on the analytical potential energy surface with its barrier in the product valley (the HCl bond length at the saddle point is only 0.08 Å longer than HCl in products while the CH bond length is 0.30 Å longer at the saddle point than in the reactants). Figure 27.7 shows the potential along the MEP and the ground-state adiabatic potential for this reaction, harmonic frequencies $\omega_i(s)$, and components $\kappa_i(s)$ of reaction-path curvature along the reaction coordinate. Although there are 11 vibrational modes orthogonal to the reaction path, only 3 have significant curvature components. Relative motion of the two heavy moieties CH_3 and Cl dominates the reaction coordinate in the reactant and product regions, while in the interaction region, where the curvature is largest, motion of the H atom between CH_3 and Cl characterizes reaction coordinate motion. The mode that couples most strongly to reaction coordinate motion mirrors this behavior and is denoted the reactive mode. It originates as a nondegenerate CH stretch in the reactants, transforms into motion that is dominated by C–Cl vibration in the region of strong coupling, and ends as an HCl stretch in the products. Note that regions of large reaction-path curvature also coincide with regions where the har-

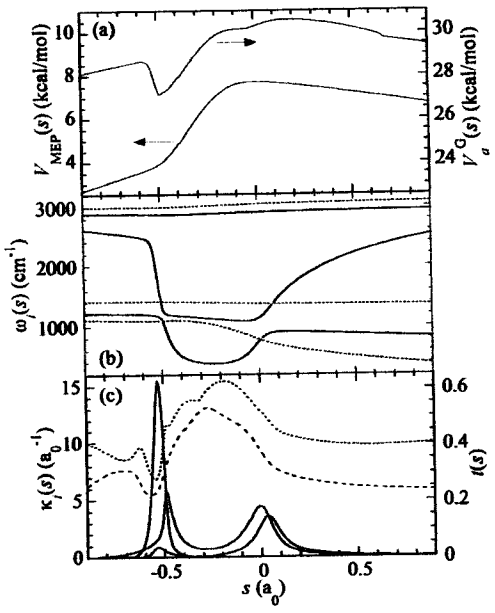

Figure 27.7 (a) Potential energy and ground-state adiabatic potential curves as a function of reaction coordinate for the Cl + CH_4 reaction using the SPES surface. (b) Nine highest harmonic frequencies for modes orthogonal to the reaction coordinate. Doubly degenerate modes are shown as dashed curves. The two lowest frequency transition modes are not shown. (c) Components of reaction-path curvature (solid lines) for 3 vibrational modes and two approximations for turning points along the curvature vector (dashed curves) as a function of reaction coordinate. Short dashed curve is the $\hat{\kappa}(s)\cdot t(s)$ approximation and the long dashed curve is $\bar{t}(s)$ (see text).

monic frequencies change rapidly and we observe crossings of modes. Because of the late barrier, the largest curvature occurs well before the saddle point (between $s = -0.6$ and $-0.4\ a_0$), where the potential along the MEP is only about half the value at the barrier maximum and the adiabatic potential exhibits a local minimum. The peak in the curvature and dip in the adiabatic potential are a result of the transformation of the reactive mode from a high-frequency CH stretching mode (2870 cm^{-1} in the reactants) to a lower frequency mode (~1300 cm^{-1} at $s = -0.5\ a_0$) with contributions from CCl motion. A second region of large curvature occurs near the saddle point where this low-frequency mode transforms into a high frequency HCl vibration (2990 cm^{-1} at products). A second mode, corresponding to a methyl umbrella mode, also shows significant coupling to the reaction coordinate, and the value of curvature coupling for this mode is larger than the reactive mode near $s = 0$). A third mode, corresponding to a high-frequency CH stretching mode throughout the reaction, exhibits much smaller, but still significant, coupling near $s = -0.5\ a_0$).

Accurate treatment of tunneling in this reaction requires consideration of how the curvature in multiple dimensions is taken into account. First we consider how the SCT method is defined to consistently treat reactions with curvature coupling in multiple modes. In SCT, we assume that the corner cutting occurs in the direction along the curvature vector $\kappa(s)$ in the space of the local vibrational coordinates Q. To emphasize this, the final version of the SCT method was originally called the centrifugal-dominant small-curvature approximation [22]. In this method, we make a local rotation of the vibrational axes so that $\kappa(s)$ lies along one of the axes, u_1, and by construction the curvature coupling in all other vibrational coordinates, u_i, $i = 2$ to $F - 1$, are zero in this coordinate system. Defining $\bar{t}(s)$ as the turning point for zero-point motion in the potential for the u_i coordinate, the effective mass in the imaginary action integral is given by the SCT expression for one mode coupled to the reaction coordinate, as written in Eq. (27.31), with $a(s)$ replaced by

$$\bar{a}(s) = \left(\sum_{i=1}^{F-1} [\kappa_i(s)]^2 \right)^{\frac{1}{2}} \bar{t}(s) \tag{27.34}$$

where F is the number of vibrational modes, $t_i(s)$ is the turning point for mode i on the concave side of the MEP. The definition of $\bar{t}(s)$ is provided in previous work for a harmonic description of the vibrational modes [22]. We illustrate here how it works for the Cl + CH_4 reaction.

As discussed above, only three modes contribute significantly to the reaction-path curvature in the Cl + CH_4 reaction, and the coupling for two of the modes is much greater than for the third. Figure 27.8 shows a contour plot of the two harmonic vibrational modes with the largest coupling where the frequencies are those at $s = -0.49\ a_0$. Turning points in these modes, $t_1(s)$ and $t_2(s)$, are indicated by the square and triangle. The direction $\hat{\kappa}(s)$, a unit vector, of the curvature-coupling vector $\kappa(s)$ is shown as a straight line and this line defines the u_1 axis. The line extends out to a value equal to $\hat{\kappa}(s) \cdot \mathbf{t}(s) = \kappa_1(s)t_1(s) + \kappa_2(s)t_2(s)$. This approximation to the turning point in u_1 (which is what one would use if one allowed independent corner cutting in every generalized normal mode) gives a value that is too

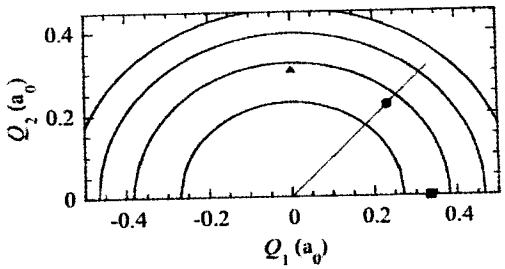

Figure 27.8 Potential energy contours for two harmonic vibrational modes, which are orthogonal to the reaction coordinate, for the Cl + CH_4 reaction at $s = -0.49\ a_0$ on the reaction coordinate. The straight line is the direction u_1 of the reaction-path curvature vector and the symbols are turning points for zero-point harmonic motion along Q_1 (square), Q_2 (triangle), and u_1 (circle).

high when compared with value of $\bar{t}(s)$ for the SCT method, which is indicated by the circle. Figure 27.7 presents a comparison of $\bar{t}(s)$ and $\hat{\kappa}(s)\cdot t(s)$ along the reaction path and shows that the value obtained using the $\hat{\kappa}(s)\cdot t(s)$ approximation is consistently larger than $\bar{t}(s)$. For systems with many modes contributing significantly to the reaction-path curvature, the overestimate of the turning point that one would obtain by allowing independent corner cutting in every generalized normal mode is even larger and unphysical. Equation (27.34) gives a consistent procedure to extend the SCT approach to multidimensional systems.

As was the case with the Cl + HBr reaction, the small skew angle and concomitant large reaction-path curvature in the Cl + CH_4 reaction require consideration of methods beyond the small-curvature approximation. It might be argued that the SCT method is adequate because the region of largest curvature falls outside the region where tunneling contributes significantly to the thermal rate constant. However, the only true test is to perform calculations that treat corner cutting more accurately for large-curvature systems. Previous work on this system has shown that the optimum tunneling paths are the straight-line paths used in the LCT method [57]. Consistent procedures have been presented for extending large-curvature methods to multidimensional systems [22, 39, 49]. In the LCG3 and LCG4 versions of the LCT method the tunneling paths are uniquely defined as straight lines between points on the MEP in the reactant and product valleys, and the key to their success is the definition of the effective potentials along these tunneling paths. As mentioned previously, the SCT and LCT methods represent approaches that are most appropriate for two extremes and the most general and optimal way to interpolate between these extremes is the least-action method. A simpler optimized tunneling (OMT) approach [23, 59] is obtained by using the SCT and LCT reaction probabilities and choosing the one that gives the largest tunneling probability at each energy. In this case the OMT probability is given by

$$p^{\mathrm{OMT}}(E) = \max\begin{Bmatrix} p^{\mathrm{SCT}}(E) \\ p^{\mathrm{LCT}}(E) \end{Bmatrix} \tag{27.35}$$

and the microcanonical optimized multidimensional tunneling (μOMT) tunneling correction factor is obtained by substituting this expression for the probability into Eq. (27.13). Rate constants and kinetic isotope effects for the Cl + CH_4 reaction, its reserve, and its isotopic variants, computed using μOMT on the potential of Corchado et al. agree well with experiment [57].

27.4 Intramolecular Hydrogen Transfer in Unimolecular Gas-phase Reactions

Intramolecular hydrogen transfer is another important class of chemical reactions that has been widely studied using transition state theory. Unimolecular gas-phase reactions are most often treated using RRKM theory [60], which combines a microcanonical transition state theory treatment of the unimolecular reaction step with models for energy redistribution within the molecule. In this presentation we will focus on the unimolecular reaction step and assume that energy redistribution is rapid, which is equivalent to the high-pressure limit of RRKM theory.

Unimolecular hydrogen transfer reactions require additional considerations beyond those discussed for bimolecular reactions. The expression for the thermal rate constant takes the same form as Eq. (27.1), but the reactant partition function per unit volume in the bimolecular expression is replaced by a unitless partition function for the vibrations and rotations of the reactant molecule. More serious considerations are required in treating quantum mechanical effects, particularly tunneling. For bimolecular reactions, quantum mechanical tunneling can be initiated by relative translational motion along the reaction coordinate or by vibrational motion in small skew-angle systems. For unimolecular reactions, vibrational motion alone promotes tunneling. For bimolecular reactions, heavy–light–heavy mass combinations require the reaction coordinate to have regions of large reaction-path curvature to connect the reaction paths in the asymptotic entrance and exit channels. (If the barrier occurs in the region of high curvature, large-curvature tunneling may dominate small-curvature tunneling.) Such a general statement cannot be made for unimolecular reactions, and the type of reaction-path curvature in unimolecular H-transfer reactions can vary from small-curvature to large-curvature.

Initiation of tunneling by vibrational motion in the reaction coordinate motion requires modification to the expression used to obtain the thermally averaged tunneling correction factor, Eq. (27.19). For unimolecular processes tunneling does not occur for a continuum of translational energies, but from discrete energy levels in the bound wells of the adiabatic potential. In this case the integral in Eq. (27.19) should be replaced by a sum over discrete states plus contributions from continuum energies above the barrier [61, 62]

$$\kappa^{VA}(T) = (k_B T)^{-1}\exp(-V^{AG}/k_B T)\sum_v \frac{d\varepsilon_v}{dv} P_Q^{AG}(\varepsilon_v)\exp(-\varepsilon_v/k_B T)$$

$$+ (k_B T)^{-1}\exp(-V^{AG}/k_B T)\int_{V^{AG}}^{\infty} dE\, P_Q^{AG}(E)\exp(-E/k_B T) \qquad (27.36)$$

where the sum is over all bound states along the reaction coordinate motion in the reactant well, ε_v is the energy of state v in the reactants, and $P_Q^{AG}(E)$ for energies above the barrier are given by Eq. (27.22) up to $2V^{AG} - E_0$ and are set to one above that energy. Equations (27.19) and (27.36) are equivalent for a sufficiently large density of states in the reactant well.

We provide two examples of intramolecular hydrogen transfer reactions in polyatomic systems to illustrate the convenience and value of VTST methods for treating these types of reactions.

27.4.1 Intramolecular H-transfer in 1,3-Pentadiene

The [1,5] sigmatropic rearrangement reaction of *cis*-1,3-pentadiene proceeds via hydrogen transfer from C-5 to C-1, and a primary kinetic isotope effect has been observed experimentally [63]. The large number of degrees of freedom (33 vibrational modes at the reactants) and types of motions involved in the rearrangement process, including torsional motions and vibrations of the carbon skeletal modes, as well as H atom motions, complicate theoretical treatment of this reaction. For this reason, approaches based on reduced-dimensional models [64] have difficulty capturing the correct dynamics of the rearrangement process. Variational transition state theory with multidimensional tunneling has been applied to this reaction in its full dimensionality to provide a complete understanding of the dynamics of the rearrangement process and the importance of tunneling in it [24, 65]. These studies used the direct dynamics approach [33, 66] in which electronic structure calculations of energies, gradients, and Hessians are performed as needed.

The reactant configuration of 1,3-pentadience is the *s-trans* conformer. Denoting the dihedral angles for C1–C2–C3–C4 and C2–C3–C4–C5 as ϕ_1 and ϕ_2, respectively, motion along the MEP out of the reactant well corresponds to rotation of ϕ_1 around the C2–C3 single bond from 180° to a value of about 30°. The change in energy for this motion along the reaction coordinate is relatively small compared to the barrier height of 39.5 kcal mol^{-1}. Once the ethylene group (C1–C2) approaches the C5 methyl group, the second dihedral angle changes in a concerted manner with ϕ_1, that is, ϕ_2 increases from a value of zero as ϕ_1 continues to decrease. The potential along the MEP is shown in Fig. 27.9, and the left most extreme of the reaction coordinate ($s = -3\ a_0$) is approximately the value of the reaction coordinate where ϕ_2 starts to change. Much closer to the saddle point (within about 0.5 a_0) the reaction coordinate motion is characterized by H-atom motion (relative to C1 and C5) accompanied by rearrangement in the C–C distances, with the largest changes in the C1–C2 and C4–C5 distances. The saddle point is a cyclic structure with C_s symmetry, the transferring H atom is equidistant from the C_1 and C_5 carbon atoms with a bent C–H–C configuration.

Analysis of the frequencies along the minimum energy path allows identification of the modes that are most strongly coupled to the reaction coordinate and have the largest participation in the tunneling process. Figure 27.9 shows all 32

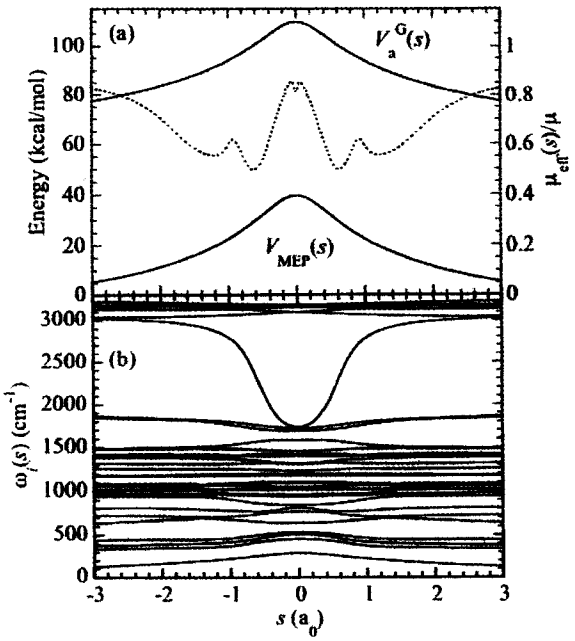

Figure 27.9 (a) Potential energy and ground-state adiabatic potential curves (solid curves) and SCT effective mass (dashed curve) as a function of reaction coordinate for the intramolecular H-tranfer in 1,3-pentadiene. (b) Harmonic frequencies for modes orthogonal to the reaction coordinate.

frequencies and the one mode that shows the most rapid change near the saddle point is that with the largest curvature coupling. This reactive mode starts as a CH vibration in reactants and transforms into the C2–C3–C4 asymmetric stretch near the saddle point. This mode accounts for the largest single component to the reaction-path curvature at the saddle point, varying from about 1/3 to 2/3 of the total contribution in the region between $s = -0.3$ and 0.3 a_0. The highest frequency modes (those above 3000 cm^{-1} at the saddle point) contribute less than a couple of percent and the lowest frequency modes (those below about 700 cm^{-1} at the saddle point) only contribute between 15 and 20% to the reaction-path curvature. This analysis shows the shortcomings of simple reduced-dimensional models of this complicated rearrangement and tunneling process. First, it is difficult to guess, *a priori*, the mode or modes that are critical for an accurate description of the multidimensional tunneling process [64]. Second, even when the dominant mode is discovered, there are 20 other modes in the range 800 to 2000 cm^{-1} that do contribute significantly to the curvature, and an accurate treatment of tunneling needs to account for motion in those degrees of freedom.

For this reaction, both LCG3 and SCT methods were applied to calculate tunneling correction factors [24]. The SCT method gave larger tunneling probabilities,

indicating that reaction-path curvature is small to intermediate for the region of the reaction coordinate over which tunneling is important. The adiabatic potential used in the SCT ground-state tunneling calculations is shown in Fig. 27.9. For temperatures around 460 K (the bottom of the range for experimental measurements) the maximum contribution to the tunneling integral occurs about 2.5 kcal mol^{-1} below the adiabatic barrier maximum. At this energy the turning points in the adiabatic potential occur for $s = \pm 0.26\ a_0$. These values are inside the two places where the maximum curvature occurs (around $s = \pm 0.6\ a_0$) and this is reflected in the values of the effective mass (also shown in Fig. 27.9), which are in the range 0.7–0.9 of the reduced mass in this region. Even with these moderate values for the effective mass, the SCT tunneling factor at 460 K is over 70% larger than the one neglecting reaction-path curvature.

27.4.2
1,2-Hydrogen Migration in Methylchlorocarbene

The 1,2-hydrogen migration in methylchlorocarbene converts it to chloroethene: $H_3CCCl \rightarrow H_2CC(H)Cl$. Calculations were carried out using direct dynamics [67]. At 365 K, tunneling lowers the gas-phase Arrhenius activation energy from 10.3 kcal mol^{-1} to 8.5 kcal mol^{-1}, and at 175 K the drop is even more dramatic, from 10.2 kcal mol^{-1} to 2.0 kcal mol^{-1}.

27.5
Liquid-phase and Enzyme-catalyzed Reactions

Placing the reagents in a liquid or an enzyme active site involves new complications. Since it is not presently practical to treat an entire condensed-phase system quantum mechanically one begins by dividing the system into two subsystems, which may be called solute and solvent, reactive system and bath, or primary subsystem and secondary subsystem. The "primary/secondary" language is often preferred because it is most general. For example, in a simple liquid-phase reaction the primary subsystem might consist of the reactive solute(s) plus one or more strongly coupled solvent molecules, and the secondary subsystem would be the rest of the solvent. In an enzyme-catalyzed reaction, the primary subsystem might be all or part of the substrate plus all or part of a cofactor and possibly a part of the enzyme and even one or a few solvent molecules, whereas the secondary subsystem would be all the rest. The solvent, bath, or secondary subsystem is sometimes called the environment.

The secondary subsystem might be treated differently from the primary one both in terms of the potential energy surface and the dynamics. For example, with regard to the former aspect, the primary subsystem might be treated by a quantum mechanical electronic structure calculation, and the secondary subsystem might be treated by molecular mechanics [68] or even approximated by an electrostatic field or a continuum model, as in implicit solvation modeling [69]. The par-

tition into primary and secondary subsystems need not be the same for the potential energy surface step and the dynamics step. Since the present chapter is mainly concerned with the dynamics, we shall assume that a potential energy function is somehow available, and when we use the "primary/secondary" language, we refer to the dynamics step. Nevertheless the strategy chosen for the dynamics may be influenced by the methods used to obtain the potential function. This is of course true even for gas-phase reactions, but the interface between the two steps often needs to be tighter when one treats condensed-phase systems, because of their greater complexity.

We will distinguish six levels of theory for treating environmental aspects of condensed-phase reactions. These levels may be arranged as follows in a hierarchy of increasingly more complete coupling of primary and secondary subsystems:

- separable equilibrium solvation VTST (SES-VTST)
- potential-of-mean-force VTST (PMF-VTST) based on a distinguished reaction-coordinate, which is also called single-reaction-coordinate PMF-VTST (SRC-PMF-VTST)
- equilibrium solvation path VTST (ESP-VTST)
- nonequilibrium solvation path VTST (NES-VTST)
- ensemble-averaged VTST with static secondary zone (EA-VTST-SSZ)
- ensemble-averaged VTST with equilibrium secondary zone (EA-VTST-ESZ)

In practical terms, though, it is easier to consider these methods in terms of two parallel hierarchies. The first contains SES, ESP, and NES; the second contains PMF-VTST, EA-VTST-SSZ, and EA-VTST-ESZ. There is, however, a complication. While the first five rungs on the ladder correspond to successively more complete theories, the final rung (ESZ) may be considered an alternative to the fifth rung (SSZ), which may be better or may be worse, depending on the physical nature of the dynamics.

An example of a system in which both solute coordinates and solvent coordinates must be treated in a balanced way is the autoionization of water. One way to describe this process is to consider a cluster of at least a half dozen water molecules as the solute, and the rest of the water molecules as the solvent. One requires solute coordinates to describe the nature of the hydrogen bond network in the solute plus at least one solvent fluctuation coordinate; the latter may describe the direction and strength of the electric field on a critical proton or protons of the solute [70] as quantified, for example, by the energy gap between arranging the solvent to solvate the reactant and arranging it to solvate the product. Molecular dynamics simulations, though, indicate that a conventional energy gap coordinate is not necessarily the best way to describe the collective solvent re-organization. A detailed comparison of different kinds of collective solvent coordinates is given elsewhere [71]. The NES-VTST method is well suited to using collective solvent coordinates whereas EA-VTST is more convenient when explicit solvent is used. The SES, ESP, and PMF methods can easily be used with either kind of treatment of the solvent.

The PMF-VTST approach may be understood in terms of a general molecular dynamics calculation of the equilibrium one-way flux from a reactant region of phase space through a dividing surface [5–7, 72, 73]. When the no-recrossing approximation is valid at the dividing surface and when one neglects quantum effects, it may be viewed as the most efficient way to calculate the rate constant from an ensemble of trajectories. However, for reactions involving hydrogenic motion in the reaction coordinate, classical mechanics is not quantitatively accurate, and the transition state formulation provides a much more convenient way to include quantum effects than does a trajectory calculation. (Note that many workers use the term "molecular dynamics" to refer to classical trajectory calculations.)

In the rest of this section we briefly review the six rungs of the condensed-phase VTST ladder. In Section 27.6 we provide two examples that illustrate the application of the general theory.

27.5.1 Separable Equilibrium Solvation

The simplest way to include solvation effects is to calculate the reaction path and tunneling paths of the solute in the gas phase and then add the free energy of solvation at every point along the reaction path and tunneling paths. This is equivalent to treating the Hamiltonian as separable in solute coordinates and solvent coordinates, and we call it separable equilibrium solvation (SES) [74]. Adding tunneling in this method requires a new approximation, namely the canonical mean shape (CMS) approximation [75].

The gas-phase rate constant of Eqs. (27.4) and (27.23) is replaced in the SES approximation by

$$k^{\mathrm{SES/MT}}(T) = \kappa(T) k^{\mathrm{SES}}(T) \tag{27.37}$$

and

$$k^{\mathrm{SES}}(T) = \frac{k_B T}{h} K^{\ddagger o} \min_s \exp\left\{ -\left[\Delta G_T^{\mathrm{GT},o}(s) + \Delta\Delta G_S^{o}(s|T) \right] \right\} \tag{27.38}$$

where $\Delta\Delta G_S^{o}(s|T)$ is the difference between the standard-state free energy of solvation of the generalized transition state at s and that of the reactants. The transmission coefficient is given by Eq. (27.25), and all that is done to extend the SCT, LCT, and OMT approximations from the gas phase to liquid reactions is to generalize V_1 and V_2.

In the SES approximation, V_1 is taken as

$$V_1(\mathbf{R}|T) = U(\mathbf{R}|T) \tag{27.39}$$

where **R** denotes the complete set of solute coordinates, and $U(\mathbf{R}|T)$ is the CMS potential given by

$$U(\mathbf{R}|T) = W(\mathbf{R}|T) + (1/T)\frac{\partial W(\mathbf{R}|T)}{\partial(1/T)} \tag{27.40}$$

and $W(\mathbf{R}|T)$ is the potential of mean force (PMF) on the primary subsystem, which will be called the solute in the rest of this Subsection and in Subsection 27.5.3. The PMF is defined by

$$e^{-W(\mathbf{R}'|T)/k_BT} = \left\langle e^{-H/k_BT}\delta(\mathbf{R}-\mathbf{R}')\right\rangle_T \tag{27.41}$$

where H is the total system Hamiltonian, $\delta(\mathbf{R}-\mathbf{R}')$ is a multidimensional delta function that holds the solute coordinates fixed at $\mathbf{R}'$, and $\langle L\rangle_T$ denotes a normalized average over the phase space of the entire system. Colloquially, $W(\mathbf{R}|T)$ is the free energy surface of the solute. The function $U(\mathbf{R}|T)$ is the enthalpy-like component of $W(\mathbf{R}|T)$. In practice the second term of Eq. (27.40) is harder to approximate than the first term, and we can use the zero-order CMS approximation (CMS-0), which is

$$U(\mathbf{R}|T) \equiv W(\mathbf{R}|T) \tag{27.42}$$

In the SES approximation,

$$W(\mathbf{R}|T) = V(\mathbf{R}) + \Delta G_S^\circ(\mathbf{R}|T) \tag{27.43}$$

where $\Delta G_S^\circ(\mathbf{R}|T)$ is the standard-state free energy of solvation. Since we will only need differences of W, e.g., its **R** dependence, it is not a matter of concern that different standard state choices correspond to changing the zero of $W(\mathbf{R}|T)$ by **R**-independent amounts.

Finally, the SES approximation for the effective adiabatic potential is

$$V_2(s|T) = U_{RP}(s|T) + \varepsilon_{int}^{GT}(G,s) \tag{27.44}$$

where $U_{RP}(s|T)$ is $U(\mathbf{R}|T)$ evaluated along the reaction path, and $\varepsilon_{int}^{GT}(G,s)$ is the ground-state value of the second term of Eq. (27.8) for the solute modes. As for V_1, one can use any convenient zero of energy for $V_2(s|T)$ since the results are independent of adding a quantity independent of s.

The final protocol for an SES calculation with the CMS-0 approximation reduces to the following: Calculate a gas-phase MEP and carry out generalized normal mode analyses along the MEP to obtain $\varepsilon_{int}^{GT}(G,s)$ for the solute. (In an LCT calculation one also requires $\varepsilon_{int}^{GT}(\mathbf{n}\neq G, \Lambda = G, s)$.) Now add the free energy of solvation along the MEP to find the variational transition state rate constant and tunneling paths, and add the free energy of solvation along the tunneling paths to obtain an effective potential that is used to calculate the tunneling probabilities.

27.5.2
Equilibrium Solvation Path

In the equilibrium solvation path (ESP) approximation [74, 76], we first find a potential of mean force surface for the primary subsystem in the presence of the secondary subsystem, and then we finish the calculation using this free energy surface. Notice a critical difference from the SES in that now we find the MEP on U rather than V, and we now find solute vibrational frequencies using U rather than V.

27.5.3
Nonequilibrium Solvation Path

The SES and ESP approximations include the dynamics of solute degrees of freedom as fully as they would be treated in a gas-phase reaction, but these approximations do not address the full complexity of condensed-phase reactions because they do not allow the solvent to participate in the reaction coordinate. Methods that allow this are said to include nonequilibrium solvation. A variety of ways to include nonequilibrium solvation within the context of an implicit or reduced-degree-of-freedom bath are reviewed elsewhere [69]. Here we simply discuss one very general such NES method [76–78] based on collective solvent coordinates [71, 79]. In this method one replaces the solvent with one or more collective solvent coordinates, whose parameters are fit to bulk solvent properties or molecular dynamics simulations. Then one carries out calculations just as in the gas phase but with these extra one or more degrees of freedom. The advantage of this approach is its simplicity (although there are a few subtle technical details).

A difficulty with the nonequilibrium approach is that one must estimate the time constant or time constants for solvent equilibration with the solvent. This may be estimated from solvent viscosities, from diffusion constants, or from classical trajectory calculations with explicit solvent. Estimating the time constant for solvation dynamics presents new issues because there is more than one relevant time scale [69, 80]. Fortunately, though, the solvation relaxation time seems to depend mostly on the solvent, not the solute. Thus it is very reasonable to assume it is a constant along the reaction path.

Another difficulty with the NES model is not knowing how reliable the solvent model is and having no systematic way to improve it to convergence. Furthermore this model, like the SES and ESP approximations, assumes that the reaction can be described in terms of a reaction path residing in a single free energy valley or at most a small number of such valleys. The methods discussed next are designed to avoid that assumption.

The ESP method was applied to the reaction mentioned in Subsection 27.4.2, namely 1,2-hydrogen migration in chloromethylcarbene. Tunneling contributions are found to be smaller in solution than in the gas phase, but solvation by 1,2-dichloroethane lowers the Arrhenius activation energy at 298 K from 7.7 kcal mol^{-1} to 6.0 kcal mol^{-1} [67].

27.5.4
Potential-of-mean-force Method

In the PMF method one identifies a reaction coordinate on physical grounds rather than by calculating an MEP. For example, the reaction coordinate might be

$$z = r_{DH} - r_{AH} \tag{27.45}$$

where r_{DH} is the distance from the transferred hydrogen to the donor atom, and r_{AH} is the distance from the transferred hydrogen to the acceptor atom. Then one calculates a one-dimensional potential of mean force ($W(z|T)$), and the classical mechanical rate constant for a unimolecular reaction in solution is given by Eq. (27.4) with [81]

$$\Delta G_T^{CVT,o} = \max_z [W(z|T) + W_{curv}(z|T)] - G_\xi^R \tag{27.46}$$

where $W_{curv}(z|T)$ is a kinematic contribution [81], usually small, at least when the reaction coordinate is a simple function of valence coordinates as in Eq. (27.45), and G_ξ^R [82] is the free energy of the reaction-coordinate motion of the reactant. Like the SES and ESP approximations, PMF-VTST involves a single reaction coordinate.

Even within the equilibrium-solvation approximations and neglecting recrossing effects, the classical mechanical result of Eq. (27.46) needs to be improved in two ways. First one needs to quantize the vibrations transverse to the reaction coordinate. A method for doing this has been presented [83], and including this step converts Eq. (27.46) to a quasiclassical result. Second, one must include tunneling. The inclusion of tunneling is explained in the next subsection, and it involves partitioning the system into primary and secondary subsystems. Note that any reasonable definition of the primary subsystem would include the three atoms involved in the definition of the reaction coordinate given in Eq. (27.45). Thus, in the present section, if one uses Eq. (27.45), the secondary subsystem does not participate in the reaction coordinate.

27.5.5
Ensemble-averaged Variational Transition State Theory

Ensemble-averaged VTST [82, 84] provides a much more complete treatment of condensed-phase reactions. Originally developed in the context of enzyme kinetics, it is applicable to any reaction in the liquid or solid state. First one carries out a quasiclassical PMF-VTST calculation as explained in Subsection 27.5.4. This is called stage 1, and it involves a single, distinguished reaction coordinate. Then, in what is called stage 2, one improves this result with respect to the quality of the reaction coordinate (allowing the secondary subsystem to participate), with respect to averaging over more than one reaction coordinate, and by including tunneling.

Stage 2 consists of a series of calculations, each one of which corresponds to a randomly chosen member of the transition state ensemble. For this purpose the transition state ensemble consists of phase points from the quasiclassical PMF calculation with the value of z in a narrow bin centered on the variational transition state, which is the value of z that maximizes the quantized version of the right-hand side of Eq. (27.46). In practice one uses the version of Eq. (27.46) in which quantization effects of modes orthogonal to z [83] are added to W. For each member of the transition state ensemble, one now optimizes the primary subsystem to the nearest saddle point in the field of the frozen secondary subsystem, and then one computes a minimum energy path through the isoinertial coordinates of the primary subsystem, with the secondary subsystem frozen. Based on this MEP one carries out a VTST/MT rate constant calculation, just as in the gas phase except for three differences. First, one does not need the reactant partition function. Second, one freezes the secondary subsystem throughout the entire calculation. Third, the projection operator discussed below Eq. (27.1) is replaced by one that just projects out the reaction coordinate because the frozen secondary subsystem removes translational invariance, converting the overall translations and rotations to librations. (The same simplified projection operator is also used for treating solid-state reactions [61].)

The calculations described in the previous paragraph yield, for each ensemble member ℓ, a free energy of activation profile $\Delta G_\ell^{GT}(T,s)$ and a transmission coefficient $\kappa_\ell(T)$, where $\ell = 1,2,...,L$, and L is the number of MEPs computed. The standard EA-VTST/MT result, called the static-secondary-zone result, is then given by

$$k^{\text{EA-VTST/MT}} = \gamma(T)k^{\text{QPMF}}(T) \tag{27.47}$$

where k^{QPMF} is the result from stage 1, based on the quantized PMF and identical to the result of Subsection 27.5.4, and γ is a transmission coefficient given by

$$\gamma = \frac{1}{L}\sum_{\ell=1}^{L} \Gamma_\ell(T)\kappa_\ell(T) \tag{27.48}$$

where

$$\Gamma_\ell = \exp\{-[\Delta G_\ell^{GT}(T,s_{*,\ell}) - \Delta G_\ell^{GT}(T,s_{0,\ell})]/RT\} \tag{27.49}$$

where $s_{*,\ell}$ is the value of s that maximizes $\Delta G_\ell^{GT}(T,s)$, and $s_{0,\ell}$ is the value of s corresponding to the value of z that maximizes the PMF of stage 1. The physical interpretation of Γ_ℓ is that, by using a more appropriate reaction coordinate for each secondary-zone configuration, one is correcting for recrossing of the original, less appropriate dividing surface defined by z = constant. An alternative, more expensive way to do this is by starting trajectories at the dividing surface and counting their recrossings, if any [6, 15, 72]. More expensive is not necessarily more accurate though because the trajectories may lose their quantization before they recross.

In the equilibrium-secondary-zone approximation [82, 85] we refine the effective potential along each reaction path by adding the charge in secondary-zone free energy. Thus, in this treatment, we include additional aspects of the secondary subsystem. This need not be more accurate because in many reactions the solvation is not able to adjust on the time scale of primary subsystem barrier crossing [86].

27.6 Examples of Condensed-phase Reactions

27.6.1 H + Methanol

References for a large number of SES calculations are given in a previous review [69], but there have been far fewer calculations using the ESP and NES approximations. The ESP and NES approximations based on collective solvent coordinates have, however, been applied [78] to (R1) $H + CH_3OH \rightarrow H_2 + CH_4OH$, (R2) $D + CH_3OD \rightarrow DH + CH_2OD$, and (R3) $H + CD_3OH \rightarrow HD + CD_2OH$.

The resulting rate constants for reaction (R1) are shown in Table 27.1. In this particular case the NES results are accidentally similar to the SES ones, but that is not of major importance. What is more significant is that the true equilibrium solvation results differ from the SES ones by about a factor of two, and nonequilibrium solvation decreases the rate constants in solution by more than a factor of two as compared to the equilibrium solvation effect. If the solute–solvent coupling is decreased, the NES result becomes closer to the equilibrium solvation result, and it is difficult to ascertain how realistic the best estimates of the coupling strength actually are. Perhaps more interesting though is that if the coupling is made four times stronger, the calculated rate constant drops by another factor of three. Since ionic reactions might have much stronger solute–solvent coupling than this free radical reaction, we conclude that nonequilibrium effects might be larger for many reactions in aqueous solution.

Table 27.2 shows the kinetic isotope effects [78, 87]. Although the solvation effects are smaller than for the rate constants themselves, they are not negligible.

Tab. 27.1 Rate constants (10^{-15} cm^3 molecule^{-1} s^{-1}) at various levels of dynamical theory for $H + CH_3OH \rightarrow H_2 + CH_2OH$ in aqueous solution at 298 K [78].

	Gas	SES	ESP	NES
CVT	0.7	0.9	1.9	0.81
CVT/SCT	8.3	8.7	16.6	6.5
CVT/OMT	12.9	12.7	25.9	12.4

Tab. 27.2 Kinetic isotope effects for $H + CH_3OH \rightarrow H_2 + CH_2OH$ at various levels of dynamical theory in aqueous solution at 298 K (CVT/OMT [78, 87]).

	Gas	SES	ESP	NES
R1/R2	0.68	0.48	0.51	0.37
R1/R3	21.1	21.3	20.2	19.5

Although a more recent calculation [88] indicates a barrier height about 2 kcal mol^{-1} higher than that on the potential energy surface used for these studies, the qualitative conclusions still hold if they are regarded as based on a realistic model reaction.

27.6.2 Xylose Isomerase

Xylose isomerase catalyzes a hydride transfer reaction as part of the conversion of xylose to xylulose. This reaction has been calculated [32] by the EA-VTST/MT method using Eq. (27.45) as the reaction coordinate and using $L = 5$ in Eq. (27.48). The primary zone had 32 atoms, and the secondary zone had 25 285 atoms. The average value of Γ_ℓ was 0.95. The fact that this is so close to unity indicates that the reaction coordinate of Eq. (27.45) is very reasonable for this reaction, even though the reaction coordinate is strongly coupled to a Mg–Mg breathing mode. The transmission coefficient γ was calculated to be 6.57, with about 90% of the reactive events calculated to occur by tunneling.

Calculations were also carried out for deuteride transfer. The kinetic isotope effect was calculated to be 1.80 without tunneling and 3.75 with tunneling. The latter is within the range expected from various experimental [89] determinations.

27.6.3 Dihydrofolate Reductase

The ensemble-averaged theory has also been applied to several other enzyme reactions involving transfer of a proton, hydride ion, or hydrogen atom, and the results are reviewed elsewhere [84, 90]. More recently than these reviews, the method has been applied to calculate [91] the temperature dependence of the rate constant and kinetic isotope effect for the hydride transfer catalyzed by *E. coli* dihydrofolate reductase (*ec*DHFR). In earlier work [92] we had calculated a primary KIE in good agreement with experiment [93] and also predicted a secondary KIE that turned out to be in good agreement with a later [94] experiment. In both studies [91, 92], we treated the dynamics of 31 atoms quantum mechanically. The primary KIE had also been calculated by Agarwal et al. [95], also in good agreement with experiment, but they could not calculate the secondary KIE because they treated the dynamics of only one atom quantum mechanically. In the new

work [91] we predicted the temperature dependence of the KIE and found that it is small. In previous work by other groups, new mechanisms had been invoked when temperature-independent or nearly temperature-independent KIEs had been observed. The importance of the new work [91] is not so much the actual predicted small temperature dependence of the KIE (because the quantitative results may be sensitive to improving the calculation) but rather the demonstration that even nearly temperature-independent KIEs can be accommodated by VTST/MT theory, and one need not invoke new theoretical concepts.

27.7 Another Perspective

For another perspective we mention a second approach of which the reader should be aware. In this approach the dividing surface of transition state theory is defined not in terms of a classical mechanical reaction coordinate but rather in terms of the centroid coordinate of a path integral (path integral quantum TST, or PI-QTST) [96–99] or the average coordinate of a quantal wave packet. In model studies of a symmetric reaction, it was shown that the PI-QTST approach agrees well with the multidimensional transmission coefficient approach used here when the frequency of the bath is high, but both approaches are less accurate when the frequency is low, probably due to anharmonicity [98] and the path centroid constraint [97]. However, further analysis is needed to develop practical PI-QTST-type methods for asymmetric reactions [99].

Methods like PI-QTST provide an alternative perspective on the quasithermodynamic activation parameters. In methods like this the transition state has quantum effects on reaction coordinate motion built in because the flux through the dividing surface is treated quantum mechanically throughout the whole calculation. Since tunneling is not treated separately, it shows up as part of the free energy of activation, and one does not obtain a breakdown into overbarrier and tunneling contributions, which is an informative interpretative feature that one gets in VTST/MT.

Other alternative approaches for approximating the quantum effects in VTST calculations of liquid-phase [4] and enzyme reactions [90] are reviewed elsewhere.

27.8 Concluding Remarks

In the present chapter, we have described a formalism in which overbarrier contributions to chemical reaction rates are calculated by variational transition state theory, and quantum effects on the reaction coordinate, especially multidimensional tunneling, have been included by a multidimensional transmission coefficient. The advantage of this procedure is that it is general, practical, and well validated.

It is sometimes asked if a transmission coefficient is a "correction" and therefore less fundamental than other ways of including tunneling in the activation free energy. In fact, this is not the case. The transmission coefficient is a general way to include tunneling in the flux through the dividing surface. We can see this by writing the exact rate constant as a Boltzmann average over the exact rate constants for each of the possible initial states (levels) of the system, where these initial levels are labeled as n(initial):

$$k \equiv \left\langle k_{n(\text{initial})} \right\rangle \tag{27.50}$$

We can then replace this average by an average over systems that cross the transition state in various levels of the transition state, each labeled by n(VTS):

$$k \equiv \left\langle k_{n(\text{VTS})} \right\rangle \tag{27.51}$$

We can write this as

$$k \equiv \frac{\left\langle k_{n(\text{VTS})} \right\rangle}{\left\langle k_n^{\text{TST}} \right\rangle} \left\langle k_n^{\text{TST}} \right\rangle \tag{27.52}$$

where we have multiplied and divided by an average over transition-state-theory rates for each n(VTS). The VTST rate constant can easily be written [15] in the form of the average that we have inserted into Eq. (27.52), so $\left\langle k_n^{\text{TST}} \right\rangle$ is just k^{VTST}. The fraction in Eq. (27.52) is easily recognized as the transmission coefficient κ, and therefore we have the following expression, which is exact:

$$k \equiv \kappa\, k^{\text{VTST}} \tag{27.53}$$

In practice, we approximate the exact transmission coefficient by a mean-field-type of approximation; that is we replace the ratio of averages by the ratio for an "average" or effective potential. For gas-phase reactions with small reaction-path curvature, this effective potential would just be the vibrationally adiabatic ground-state potential. In the liquid phase and enzymes we generalize this with the canonical mean-shape approximation. In any event, though, the transmission coefficient should not be thought of as a perturbation. The method used here may be thought of as an approximate full-dimensional quantum treatment of the reaction rate.

At the present stage of development, we have well validated methods available for calculating reactive rates of hydrogen atom, proton, and hydride transfer reactions in both gaseous and condensed phases, including reliable methods for multidimensional tunneling contributions. The accuracy of calculated rate constants is often limited more by the remaining uncertainties in potential energy surfaces and practical difficulties in including anharmonicity than by the dynamical formalism *per se*.

Acknowledgments

This work was supported in part at both Pacific Northwest National Laboratory (PNNL) and the University of Minnesota (UM) by the Division of Chemical Sciences, Office of Basic Energy Sciences, U. S. Department of Energy (DOE), and it was supported in part (condensed-phase dynamics) at the University of Minnesota by the National Science Foundation. Battelle operates PNNL for DOE.

References

1 H. Eyring, *J. Chem. Phys.* 3 (1935) 107; S. Glasstone, K. J. Laidler, H. Eyring, *The Theory of Rate Processes*, McGraw-Hill, New York, 1941.

2 H. Eyring, Trans. Faraday Soc. 34 (1938) 41; B. C. Garrett, D. G. Truhlar, in *Encyclopedia of Computational Chemistry*, P. v. R. Schleyer, N. L. Allinger, T. Clark, J. Gasteiger, P. A. Kollman, H. F. Schaefer, III (Eds.), John Wiley & Sons, Chichester, 1998.

3 E. Wigner, *Trans. Faraday Soc.* 34 (1938) 29.

4 D. G. Truhlar, W. L. Hase, J. T. Hynes, *J. Phys. Chem.* 87 (1983) 2664; D. G. Truhlar, B. C. Garrett, S. J. Klippenstein, *J. Phys. Chem.* 100 (1996) 12771.

5 E. Wigner, *J. Chem. Phys.* 5 (1937) 720; J. Horiuti, *Bull. Chem. Soc. Jpn.* 13 (1938) 210; J. C. Keck, *J. Chem. Phys.* 32 (1960) 1035; D. G. Truhlar, B. C. Garrett, *Annu. Rev. Phys. Chem.* 35 (1984) 159.

6 J. C. Keck, *Adv. Chem. Phys.* 13 (1967) 85.

7 B. C. Garrett, D. G. Truhlar, *J. Phys. Chem.* 83 (1979) 1052.

8 E. Wigner, *Z. Phys. Chem. B* 19 (1932) 203.

9 R. P. Bell, *The Proton in Chemistry*, Chapman and Hall, London, 1973.

10 D. G. Truhlar, A. Kuppermann, *Chem. Phys. Lett.* 9 (1971) 269.

11 W. H. Miller, *Acc. Chem. Res.* 9 (1976) 306.

12 J. O. Hirschfelder, E. Wigner, *J. Chem. Phys.* 7 (1939) 616; H. Eyring, J. Walter, G. E. Kimball, *Quantum Chemistry*, Wiley, New York, 1944; R. A. Marcus, *J. Chem. Phys.* 43 (1965) 1598; R. A. Marcus, *J. Chem. Phys.* 45 (1966) 4450; D. G. Truhlar, *J. Chem. Phys.* 53 (1970) 2041.

13 G. L. Hofacker, *Z. Naturforsch. A* 18 (1963) 607.

14 R. A. Marcus, *J. Chem. Phys.* 45 (1966) 4493.

15 B. C. Garrett, D. G. Truhlar, *J. Phys. Chem.* 83 (1979) 1079.

16 B. C. Garrett, D. G. Truhlar, R. S. Grev, A. W. Magnuson, *J. Phys. Chem.* 84 (1980) 1730.

17 R. T. Skodje, D. G. Truhlar, B. C. Garrett, *J. Phys. Chem.* 85 (1981) 3019.

18 R. T. Skodje, D. G. Truhlar, B. C. Garrett, *J. Chem. Phys.* 77 (1982) 5955.

19 B. C. Garrett, D. G. Truhlar, A. F. Wagner, T. H. Dunning, Jr., *J. Chem. Phys.* 78 (1983) 4400; D. K. Bondi, J. N. L. Connor, B. C. Garrett, D. G. Truhlar, *J. Chem. Phys.* 78 (1983) 5981.

20 B. C. Garrett, D. G. Truhlar, *J. Chem. Phys.* 79 (1983) 4931.

21 B. C. Garrett, T. Joseph, T. N. Truong, D. G. Truhlar, *Chem. Phys.* 136 (1989) 271.

22 D.-h. Lu, T. N. Truong, V. S. Melissas, G. C. Lynch, Y.-P. Liu, B. C. Garrett, R. Steckler, A. D. Isaacson, S. N. Rai, G. C. Hancock, J. G. Lauderdale, T. Joseph, D. G. Truhlar, *Comput. Phys. Commun.* 71 (1992) 235.

23 Y.-P. Liu, D.-h. Lu, A. Gonzalez-Lafont, D. G. Truhlar, B. C. Garrett, *J. Am. Chem. Soc.* 115 (1993) 7806.

24 Y.-P. Liu, G. C. Lynch, T. N. Truong, D.-h. Lu, D. G. Truhlar, B. C. Garrett, *J. Am. Chem. Soc.* 115 (1993) 2408.

25 R. A. Marcus, M. E. Coltrin, *J. Chem. Phys.* 67 (1977) 2609.

26 C. J. Walsh, *Enzyme Reaction Mechanisms*, Freeman, New York, 1979.

27 D. G. Truhlar, R. E. Wyatt, *Annu. Rev. Phys. Chem.* 27 (1976) 1.

28 H. S. Johnston, *Gas Phase Reaction Rate Theory*, Ronald, New York, 1966.

29 L. Melander, *Isotope Effects on Reaction Rates*, Ronald Press, New York, 1960; L. Melander, W. H. Saunders, *Reaction Rates of Isotopic Molecules*, Krieger Publishing, Malabar, FL, 1987.

30 J. Bigeleisen, M. Wolfsberg, *Adv. Chem. Phys.* 1 (1958) 15.

31 B. C. Garrett, D. G. Truhlar, *J. Am. Chem. Soc.* 102 (1980) 2559.

32 M. Garcia-Viloca, C. Alhambra, D. G. Truhlar, J. Gao, *J. Comput. Chem.* 24 (2003) 177.

33 D. G. Truhlar, M. S. Gordon, *Science* 249 (1990) 491.

34 B. C. Garrett, D. G. Truhlar, *J. Chem. Phys.* 70 (1979) 1593.

35 R. E. J. Weston, *J. Chem. Phys.* 31 (1959) 892; I. Shavitt, *J. Chem. Phys.* 49 (1968) 4048; R. A. Marcus, *J. Chem. Phys.* 49 (1968) 2617; K. Fukui, in *The World of Quantum Chemistry*, R. Daudel, B. Pullman (Eds.), Reidel, Dordrecht, 1974; H. F. Schaefer, III, *Chem. Brit.* 11 (1975) 227.

36 D. G. Truhlar, A. Kuppermann, *J. Am. Chem. Soc.* 93 (1971) 1840.

37 W. H. Miller, N. C. Handy, J. E. Adams, *J. Chem. Phys.* 72 (1980) 99.

38 A. D. Isaacson, D. G. Truhlar, *J. Chem. Phys.* 76 (1982) 1380.

39 D. G. Truhlar, A. D. Isaacson, B. C. Garrett, in *Theory of Chemical Reaction Dynamics*, M. Baer (Ed.), CRC Press, Boca Raton, FL, 1985.

40 C. F. Jackels, Z. Gu, D. G. Truhlar, *J. Chem. Phys.* 102 (1995) 3188.

41 S. J. Klippenstein, R. A. Marcus, *J. Chem. Phys.* 87 (1987) 3410; J. Villa, D. G. Truhlar, *Theor. Chem. Acc.* 97 (1997) 317; P. L. Fast, D. G. Truhlar, *J. Chem. Phys.* 109 (1998) 3721; J. R. Pliego, W. B. De Almeida, *Phys. Chem. Chem. Phys.* 1 (1999) 1031.

42 B. C. Garrett, D. G. Truhlar, *J. Chem. Phys.* 72 (1980) 3460; G. A. Natanson, B. C. Garrett, T. N. Truong, T. Joseph, D. G. Truhlar, *J. Chem. Phys.* 94 (1991) 7875; G. A. Natanson, *Theor. Chem. Acc.* 112 (2004) 68.

43 A. D. Isaacson, *J. Phys. Chem. A* 110 (2006) 379.

44 R. A. Marcus, *J. Chem. Phys.* 46 (1967) 959; R. A. Marcus, *J. Chem. Phys.* 49 (1968) 2610.

45 D. G. Truhlar, B. C. Garrett, *J. Phys. Chem. A* 107 (2003) 4006.

46 R. A. Marcus, *J. Chem. Phys.* 41 (1964) 2614; G. L. Hofacker, N. Rösch, *Ber. Bunsen- Ges. Phys. Chem.* 77 (1973) 661.

47 D. C. Chatfield, R. S. Friedman, D. G. Truhlar, B. C. Garrett, D. W. Schwenke, *J. Am. Chem. Soc.* 113 (1991) 486; D. C. Chatfield, R. S. Friedman, D. W. Schwenke, D. G. Truhlar, *J. Phys. Chem.* 96 (1992) 2414; D. C. Chatfield, R. S. Friedman, S. L. Mielke, G. C. Lynch, T. C. Allison, D. G. Truhlar, D. W. Schwenke, in *Dynamics of Molecules and Chemical Reactions*, R. E. Wyatt, J. Z. H. Zhang (Eds.), Marcel Dekker, New York, 1996, p. 323.

48 J. N. L. Connor, *Mol. Phys.* 15 (1968) 37; B. C. Garrett, D. G. Truhlar, *J. Phys. Chem.* 83 (1979) 2921.

49 A. Fernandez-Ramos, D. G. Truhlar, *J. Chem. Phys.* 114 (2001) 1491.

50 D. G. Truhlar, C. J. Horowitz, *J. Chem. Phys.* 68 (1978) 2466.

51 A. A. Westenberg, N. De Haas, *J. Chem. Phys.* 47 (1967) 1393; K. A. Quickert, D. J. Leroy, *J. Chem. Phys.* 53 (1970) 1325; I. D. Reid, L. Y. Lee, D. M. Garner, D. J. Arseneau, M. Senba, D. G. Fleming, *Hyperfine Interact.* 32 (1986) 801.

52 B. C. Garrett, D. G. Truhlar, *J. Phys. Chem.* 83 (1979) 1915; D. G. Truhlar, A. D. Isaacson, R. T. Skodje, B. C. Garrett, *J. Phys. Chem.* 86 (1982) 2252; D. G. Truhlar, *J. Comput. Chem.* 12 (1991) 266.

53 B. C. Garrett, D. G. Truhlar, *J. Chem. Phys.* 81 (1984) 309.

54 V. K. Babamov, V. Lopez, R. A. Marcus, *Chem. Phys. Lett.* 101 (1983) 507; V. K. Babamov, V. Lopez, R. A. Marcus, *J. Chem. Phys.* 78 (1983) 5621;

V. K. Babamov, V. Lopez, R. A. Marcus, *J. Chem. Phys.* 80 (1984) 1812.

55 B. C. Garrett, N. Abusalbi, D. J. Kouri, D. G. Truhlar, *J. Chem. Phys.* 83 (1985) 2252.

56 T. C. Allison, D. G. Truhlar, in *Modern Methods for Multidimensional Dynamics Computations in Chemistry*, D. L. Thompson (Ed.), World Scientific, Singapore, 1998.

57 J. C. Corchado, D. G. Truhlar, J. Espinosa-Garcia, *J. Chem. Phys.* 112 (2000) 9375.

58 M. S. Zahniser, B. M. Berquist, F. Kaufman, *Int. J. Chem. Kinet.* 10 (1978) 15; M. L. Pohjonen, J. Koskikallio, *Acta Chem. Scand. Ser. A* 33 (1979) 449; J. J. Russell, J. A. Seetula, S. M. Senkan, D. Gutman, *Int. J. Chem. Kinet.* 20 (1988) 759; T. J. Wallington, M. D. Hurley, *Chem. Phys. Lett.* 189 (1992) 437; W. R. Simpson, A. J. Orr-Ewing, R. N. Zare, *Chem. Phys. Lett.* 212 (1993) 163; Y. Matsumi, K. Izumi, V. Skorokhodov, M. Kawasaki, N. Tanaka, *J. Phys. Chem. A* 101 (1997) 1216; A. J. Orr-Ewing, W. R. Simpson, T. P. Rakitzis, S. A. Kandel, R. N. Zare, *J. Chem. Phys.* 106 (1997) 5961; S. A. Kandel, R. N. Zare, *J. Chem. Phys.* 109 (1998) 9719; G. D. Boone, F. Agyin, D. J. Robichaud, F. M. Tao, S. A. Hewitt, *J. Phys. Chem. A* 105 (2001) 1456.

59 D. G. Truhlar, D.-h. Lu, S. C. Tucker, X. G. Zhao, A. Gonzalez-Lafont, T. N. Truong, D. Maurice, Y.-P. Liu, G. C. Lynch, in *Isotope Effects in Gas-Phase Chemistry*, J. A. Kay (Ed.), American Chemical Society, Washington, D. C., 1992.

60 R. G. Gilbert, S. C. Smith, *Theory of Unimolecular and Recombination Reactions*, Blackwell, Oxford, 1990; T. Baer, W. L. Hase, *Unimolecular Reaction Dynamics*, Oxford University Press, New York, 1996.

61 J. G. Lauderdale, D. G. Truhlar, *Surf. Sci.* 164 (1985) 558.

62 G. C. Hancock, C. A. Mead, D. G. Truhlar, A. J. C. Varandas, *J. Chem. Phys.* 91 (1989) 3492; B. M. Rice, B. C. Garrett, M. L. Koszykowski, S. M. Foiles, M. S. Daw, *J. Chem. Phys.* 92 (1990) 775; S. E. Wonchoba, W. P. Hu, D. G. Truhlar, *Phys. Rev. B* 51 (1995) 9985; P. S. Zuev, R. S. Sheridan, T. V. Albu, D. G. Truhlar, D. A. Hrovat, W. T. Borden, *Science* 299 (2003) 867.

63 W. R. Roth and J. König, *Liebigs Ann. Chem.* 699 (1966) 24.

64 L. Chantranupong, T. A. Wildman, *J. Am. Chem. Soc.* 112 (1990) 4151.

65 Y. Kim, J. C. Corchado, J. Villa, J. Xing, D. G. Truhlar, *J. Chem. Phys.* 112 (2000) 2718.

66 K. K. Baldridge, M. S. Gordon, R. Steckler, D. G. Truhlar, *J. Phys. Chem.* 93 (1989) 5107; B. C. Garrett, M. L. Koszykowski, C. F. Melius, M. Page, *J. Phys. Chem.* 94 (1990) 7096; D. G. Truhlar, in *The Reaction Path in Chemistry: Current Approaches and Perspectives*, D. Heidrich (Ed.), Kluwer, Dordrecht, 1995.

67 T. V. Albu, B. J. Lynch, D. G. Truhlar, A. C. Goren, D. A. Hrovat, W. T. Borden, R. A. Moss, *J. Phys. Chem. A* 106 (2002) 5323.

68 J. Gao, M. A. Thompson, *Combined Quantum Mechanical and Molecular Mechanical Methods*, American Chemical Society, Washington, DC, 1998; H. Lim, D. G. Truhlar, *Theor. Chem. Acc.* in press, online DOI: 10.1007/s00214-006-0143-z.

69 C. J. Cramer, D. G. Truhlar, *Chem. Rev.* 99 (1999) 2161.

70 R. A. Marcus, *J. Chem. Phys.* 24 (1956) 966; P. L. Geissler, C. Dellago, D. Chandler, J. Hutter, M. Parrinello, *Science* 291 (2001) 2121.

71 G. K. Schenter, B. C. Garrett, D. G. Truhlar, *J. Phys. Chem. B* 105 (2001) 9672.

72 C. H. Bennett, in *Algorithms for Chemical Computation*, R. E. Christofferson (Ed.) American Chemical Society, Washington, DC, 1977.

73 K. Hinsen, B. Roux, *J. Chem. Phys.* 106 (1997) 3567.

74 Y.-Y. Chuang, C. J. Cramer, D. G. Truhlar, *Int. J. Quantum Chem.* 70 (1998) 887.

75 D. G. Truhlar, Y.-P. Liu, G. K. Schenter, B. C. Garrett, *J. Phys. Chem.* 98 (1994) 8396.

76 B. C. Garrett, G. K. Schenter, *Int. Rev. Phys. Chem.* 13 (1994) 263.

77 B. C. Garrett, G. K. Schenter, in *Structure and Reactivity in Aqueous Solution*, C. J. Cramer, D. G. Truhlar (Eds.), American Chemical Society, Washington, DC, 1994.

78 Y.-Y. Chuang, D. G. Truhlar, *J. Am. Chem. Soc.* 121 (1999) 10157.

79 S. Lee, J. T. Hynes, *J. Chem. Phys.* 88 (1988) 6863; D. G. Truhlar, G. K. Schenter, B. C. Garrett, *J. Chem. Phys.* 98 (1993) 5756; M. V. Basilevsky, G. E. Chudinov, D. V. Napolov, *J. Phys. Chem.* 97 (1993) 3270.

80 I. Ohmine, H. Tanaka, *J. Chem. Phys.* 93 (1990) 8138; G. K. Schenter, R. P. McRae, B. C. Garrett, *J. Chem. Phys.* 97 (1992) 9116; M. Maroncelli, *J. Mol. Liq.* 57 (1993) 1; M. Maroncelli, V. P. Kumar, A. Papazyan, *J. Phys. Chem.* 97 (1993) 13; M. Cho, G. R. Fleming, S. Saito, I. Ohmine, R. M. Stratt, *J. Chem. Phys.* 100 (1994) 6672; M. F. Ruiz-Lopez, A. Oliva, I. Tunon, J. Bertran, *J. Phys. Chem. A* 102 (1998) 10728; B. Bagchi, R. Biswas, *Adv. Chem. Phys.* 109 (1999) 207; J. Li, C. J. Cramer, D. G. Truhlar, *Int. J. Quantum Chem.* 77 (2000) 264.

81 G. K. Schenter, B. C. Garrett, D. G. Truhlar, *J. Chem. Phys.* 119 (2003) 5828.

82 C. Alhambra, J. Corchado, M. L. Sanchez, M. Garcia-Viloca, J. Gao, D. G. Truhlar, *J. Phys. Chem. B* 105 (2001) 11326.

83 M. Garcia-Viloca, C. Alhambra, D. G. Truhlar, J. Gao, *J. Chem. Phys.* 114 (2001) 9953.

84 D. G. Truhlar, J. Gao, C. Alhambra, M. Garcia-Viloca, J. Corchado, M. L. Sanchez, J. Villa, *Acc. Chem. Res.* 35 (2002) 341; D. G. Truhlar, J. L. Gao, M. Garcia-Viloca, C. Alhambra, J. Corchado, M. L. Sanchez, T. D. Poulsen, *Int. J. Quantum Chem.* 100 (2004) 1136.

85 T. D. Poulsen, M. Garcia-Viloca, J. Gao, D. G. Truhlar, *J. Phys. Chem. B* 107 (2003) 9567.

86 G. van der Zwan, J. T. Hynes, *J. Chem. Phys.* 78 (1983) 4174; J. T. Hynes, in *Solvent Effects and Chemical Reactivity*, O. Tapia, J. Bertrán (Eds.), Kluwer, Dordrecht, 1996.

87 Y.-Y. Chuang, M. L. Radhakrishnan, P. L. Fast, C. J. Cramer, D. G. Truhlar, *J. Phys. Chem. A* 103 (1999) 4893.

88 J. Z. Pu, D. G. Truhlar, *J. Phys. Chem. A* 109 (2005) 773.

89 C. Lee, M. Bagdasarian, M. Meng, J. G. Zeikus, *J. Biol. Chem.* 265 (1990) 19082; H. van Tilbeurgh, J. Jenkins, M. Chiadmi, J. Janin, S. J. Wodak, N. T. Mrabet, A.-M. Lambeir, *Biochemistry* 31 (1992) 5467; P. B. M. van Bastelaere, H. L. M. Kerstershilderson, A.-M. Lambeir, *Biochem. J.* 307 (1995) 135.

90 J. Gao, D. G. Truhlar, *Annu. Rev. Phys. Chem.* 53 (2002) 467.

91 J. Pu, S. Ma, J. Gao, D. G. Truhlar, *J. Phys. Chem. B* 109 (2005) 8851.

92 M. Garcia-Viloca, D. G. Truhlar, J. L. Gao, *Biochemistry* 42 (2003) 13558.

93 C. A. Fierke, K. A. Johnson, S. J. Benkovic, *Biochemistry* 26 (1987) 4085.

94 R. S. Sikorski, L. Wang, K. A. Markham, P. T. R. Rajagopalan, S. J. Benkovic, A. Kohen, *J. Am. Chem. Soc.* 126 (2004) 4778.

95 P. K. Agarwal, S. R. Billeter, S. Hammes-Schiffer, *J. Phys. Chem. B* 106 (2002) 3283.

96 M. J. Gillan, *J. Phys. C* 20 (1987) 3621; G. A. Voth, D. Chandler, W. H. Miller, *J. Chem. Phys.* 91 (1989) 7749; G. R. Haynes, G. A. Voth, *Phys. Rev. A* 46 (1992) 2143; G. A. Voth, *J. Phys. Chem.* 97 (1993) 8365; M. Messina, G. K. Schenter, B. C. Garrett, *J. Chem. Phys.* 98 (1993) 8525; G. K. Schenter, G. Mills, H. Jónsson, *J. Chem. Phys.* 101 (1994) 8964; G. Mills, G. K. Schenter, D. E. Makarov, H. Jonsson, *Chem. Phys. Lett.* 278 (1997) 91.

97 R. P. McRae, G. K. Schenter, B. C. Garrett, G. R. Haynes, G. A. Voth, G. C. Schatz, *J. Chem. Phys.* 97 (1992) 7392.

98 R. P. McRae, B. C. Garrett, *J. Chem. Phys.* 98 (1993) 6929.

99 S. Jang, C. D. Schwieters, G. A. Voth, *J. Phys. Chem. A* 103 (1999) 9527.